Advances in Differential Equations and Control Processes 2026, 33(3), 4562.
doi: https://doi.org/10.59400/adecp4562

Article

Accurate computational study between spectral and wavelet methods for fractional differential equations

Hassan Zedan* , **Nada Okasha**

Department of Mathematics, Faculty of Science, Kafrelsheikh University, Kafr El Sheikh 33516, Egypt; nada_adel@sci.kfs.edu.eg

*** Corresponding author:** Hassan Zedan, hassan.zedan@sci.kfs.edu.eg

CITATION

Zedan H, Okasha N. Accurate computational study between spectral and wavelet methods for fractional differential equations. Advances in Differential Equations and Control Processes. 2026; 33(3): 4562. https://doi.org/10.59400/adecp4562

ARTICLE INFO

Received: 26 June 2026
Revised: 13 August 2026
Accepted: 20 August 2026
Available online: 7 September 2027

Abstract: This paper compares three numerical schemes for Caputo fractional differential equations: the Shifted Chebyshev Tau Method (SCTM), the Shifted Chebyshev Collocation Method (SCCM), and the Haar Wavelet Collocation Method (HWCM). In the two Chebyshev schemes, the unknown solution is approximated by shifted Chebyshev polynomials, whereas the Haar formulation uses localized piecewise-constant basis functions and fractional integration matrices. Each method reduces the governing equation to a finite algebraic system. The original contribution is a controlled like-for-like comparison in which the three formulations use the same numbers of unknowns, common independent test grids, and the same accuracy, conditioning, sparsity, and timing diagnostics. Six benchmark problems with known exact solutions are examined using the balanced approximation sizes $N = 4, 8, 16, 32$. The first five examples have smooth polynomial solutions. SCTM and SCCM recover the exact profiles to the adopted working precision whenever the exact polynomial lies in the selected approximation space. The sixth example has the nonpolynomial solution $u(x) = x^{5/2}$, whose third derivative is unbounded at the left endpoint, and therefore provides a genuine low-regularity convergence test. At $N = 32$, the maximum errors of SCTM and SCCM are 4.39523×10^{-6} and 4.31475×10^{-6}, respectively, whereas HWCM gives 4.33493×10^{-2}. The results show that the Chebyshev methods provide the highest accuracy for the problems studied, SCCM generally achieves this accuracy with a lower assembly cost than SCTM, and HWCM produces better-conditioned and less dense systems with generally first-order-type convergence.

Keywords: fractional differential equations; Caputo fractional derivative; Shifted Chebyshev Tau Method; Shifted Chebyshev Collocation Method; Haar Wavelet Collocation Method; operational matrices; low-regularity benchmark; convergence analysis

1. Introduction

Fractional differential equations are widely used to describe systems whose present behavior depends on their previous states. This memory effect distinguishes fractional models from classical integer-order models and explains their use in viscoelasticity, anomalous diffusion, signal processing, control systems, heat transfer, and several other applied fields [1,2].

Exact solutions are available for only a limited class of fractional differential equations. The analysis becomes more difficult when the model contains several fractional derivatives, variable coefficients, nonlinear terms, or complicated initial and boundary conditions. Numerical methods are therefore needed for many fractional

problems of practical interest [3–7].

Operational-matrix methods provide a convenient way to obtain numerical approximations. The unknown solution is expanded in a finite set of basis functions, and the required fractional operators are replaced by their corresponding matrix representations. Let $\Phi(x)$ denote a vector of basis functions. A truncated approximation may be written as

$$u_N(x) = C^T \Phi(x),$$

where C^T contains the unknown expansion coefficients. Substitution of the approximation and the operational matrices into the governing equation produces a finite algebraic system for these coefficients [8–10]. Related operational-matrix formulations are reported in the literature [11–13].

Operational-matrix formulations based on Jacobi-type functions have also been developed for ordinary and fractional differential equations [10, 13–15].

The problems considered in this study include linear multi-term fractional differential equations of the form

$$^{C}D^{\nu}u(x) + \sum_{j=1}^{k} \gamma_j \, {}^{C}D^{\beta_j}u(x) + \gamma_{k+1}u(x) = g(x),$$

where $^{C}D^{\nu}$ and $^{C}D^{\beta_j}$ denote Caputo fractional derivatives. The Caputo definition is adopted because the initial conditions can be expressed in the usual form used for classical differential equations [1, 2].

The numerical formulation depends strongly on the selected basis. Shifted Chebyshev polynomials provide a global polynomial representation on a finite interval [16, 17]. They have been used in spectral, collocation, and operational-matrix methods for several types of fractional differential equations [5, 8, 9, 12, 18].

Recent Chebyshev-based studies include collocation and related polynomial treatments of fractional models [19–22].

Two shifted Chebyshev formulations are considered here. In the Shifted Chebyshev Tau Method (SCTM), the unknown coefficients are determined from weighted residual equations. In the Shifted Chebyshev Collocation Method (SCCM), the residual is imposed directly at selected shifted Chebyshev nodes. Since the two methods use the same polynomial basis, their comparison shows how the choice between projection and collocation affects the resulting numerical system and its computational cost.

Haar wavelets provide a localized alternative to global polynomial bases. Their basis functions are piecewise constant and have compact support [23, 24]. Haar operational matrices and collocation formulations have been applied to fractional differential equations [25–28]. Other related Haar-based algorithms are reported in the literature [29–32].

Haar formulations have also been developed for variable-order and fractional integro-differential systems [33–35]. Related wavelet operational-matrix approaches for fractional equations are reported in the literature [36–38]. Error and convergence properties of Haar-based fractional approximations have also been examined [39, 40].

In the Haar Wavelet Collocation Method (HWCM), the highest required derivative is expanded in the Haar basis. The solution and the remaining derivatives are then reconstructed using fractional integration matrices together with the prescribed initial or boundary conditions.

Spectral and wavelet operational-matrix methods have been examined in many separate studies. Direct comparisons, however, are often based on different equations, approximation sizes, test grids, or error measures. It is then difficult to determine whether the observed differences arise from the approximation basis, the enforcement procedure, or the numerical settings. The present work addresses this issue by applying the three methods with the same numbers of unknowns and evaluating their results on the same independent test grids.

The choice of SCTM, SCCM, and HWCM provides a controlled comparison between two global shifted Chebyshev formulations and one localized wavelet formulation. SCTM and SCCM share the same trial space but use different residual-enforcement procedures. HWCM instead uses compactly supported functions and fractional integration matrices.

Legendre-, Jacobi-, Bernstein-, and spline-based formulations are not included in the numerical comparison because the present study is designed to isolate the effect of residual enforcement within a common shifted Chebyshev trial space and then compare that global setting with a localized Haar formulation under identical numerical conditions. The aim is therefore not to rank every available operational-matrix method, but to identify the numerical and algebraic differences among the three selected formulations.

The main objective of this work is to compare:

- Shifted Chebyshev Tau Method (SCTM);
- Shifted Chebyshev Collocation Method (SCCM);
- Haar Wavelet Collocation Method (HWCM).

The comparison includes the approximation procedure, the construction of the operational matrices, the form of the algebraic systems, maximum and RMS errors, observed convergence rates, equation residuals, condition numbers, matrix densities, and computational times. A balanced study is carried out using

$$N \in \{4, 8, 16, 32\},$$

with the same number of unknowns for each method. The numerical errors are evaluated on a common independent test grid.

Six benchmark problems with known exact solutions are considered. Examples 1–5 have smooth polynomial solutions. They illustrate the finite-dimensional polynomial reproduction achieved by the shifted Chebyshev methods whenever the exact solution belongs to the selected approximation space. Example 6 has the nonpolynomial exact solution

$$u(x) = x^{5/2},$$

whose third derivative becomes unbounded as $x \to 0^+$. This low-regularity example

gives nonzero errors for all three methods and allows their actual convergence behavior to be compared.

The paper is organized as follows. Section 2 introduces the required concepts of fractional calculus and the regularity assumptions. Section 3 presents the Shifted Chebyshev Tau and Collocation Methods. Section 4 describes the Haar Wavelet Collocation Method. Section 5 summarizes the computational procedure and its main costs. The common computational settings and error measures are then introduced before Section 7, which presents the six benchmark problems and their numerical results. Section 8 compares the matrix structures, conditioning, sparsity, and computational behavior. Section 9 summarizes the main differences among the methods. Finally, Sections 10 and 11 present the comparative discussion and the conclusions, respectively.

2. Preliminaries of fractional calculus

2.1. Riemann–Liouville fractional integral

The Riemann–Liouville fractional integral of order $\alpha > 0$ for a function $u(x)$ is defined by Podlubny [1] and Kilbas et al. [2]

$$J^{\alpha}u(x) = \frac{1}{\Gamma(\alpha)} \int_0^x (x-t)^{\alpha-1} u(t)\, dt, \qquad x > 0. \tag{1}$$

2.2. Caputo fractional derivative

For $m \in \mathbb{N}$ and $m-1 < \alpha \leq m$, assume that $u^{(m-1)}$ is absolutely continuous on the computational interval and that $u^{(m)}$ is integrable. The Caputo fractional derivative of order α is defined by Podlubny [1] and Kilbas et al. [2]

$${}^{C}D^{\alpha}u(x) = J^{m-\alpha}\left(\frac{d^m u(x)}{dx^m}\right). \tag{2}$$

For $m-1 < \alpha < m$, this definition can also be written as

$${}^{C}D^{\alpha}u(x) = \frac{1}{\Gamma(m-\alpha)} \int_0^x (x-t)^{m-\alpha-1} u^{(m)}(t)\, dt. \tag{3}$$

When $\alpha = m$, the Caputo derivative reduces to the classical integer-order derivative:

$${}^{C}D^{m}u(x) = u^{(m)}(x). \tag{4}$$

For a monomial x^r, where $r = 0, 1, 2, \ldots$, the Caputo fractional derivative satisfies

$${}^{C}D^{\alpha}x^r = \begin{cases} 0, & r < \lceil \alpha \rceil, \\ \dfrac{\Gamma(r+1)}{\Gamma(r-\alpha+1)} x^{r-\alpha}, & r \geq \lceil \alpha \rceil. \end{cases} \tag{5}$$

2.3. General fractional differential equation

A general multi-term fractional differential equation may be written as

$$F\left(x, u(x), {}^{C}D^{\alpha_1}u(x), {}^{C}D^{\alpha_2}u(x), \ldots, {}^{C}D^{\alpha_s}u(x)\right) = 0, \tag{6}$$

subject to suitable initial or boundary conditions. Equations (1)–(6) provide the fractional-calculus framework used in the sequel.

2.4. Regularity assumptions

For each noninteger fractional order α_j, let $m_j = \lceil \alpha_j \rceil$, so that

$$m_j - 1 < \alpha_j < m_j.$$

Throughout this study, the solution is assumed to satisfy, for every fractional order appearing in the governing equation,

$$u \in C^{m_j-1}[0, L], \quad u^{(m_j-1)} \in AC[0, L], \quad u^{(m_j)} \in L^1(0, L), \quad j = 1, 2, \ldots, s, \tag{7}$$

where $AC[0, L]$ denotes the space of absolutely continuous functions on $[0, L]$. These conditions ensure that the Caputo fractional derivatives appearing in the governing equations are well defined [1,2].

The coefficient functions and forcing terms are assumed to possess sufficient regularity for the residual equations, weighted projection integrals, and collocation evaluations to exist. The corresponding initial or boundary value problems are also assumed to admit unique solutions in the stated regularity class. For the six benchmark problems considered here, the stated exact solutions are verified directly by substitution into the governing equations and the prescribed conditions.

The assumptions are imposed according to the derivative orders appearing in each problem and do not require additional higher-order smoothness. In particular, the exact solution of Example 6 satisfies

$$u_{\text{exact}}(x) = x^{5/2} \in C^2[0, 1], \qquad u_{\text{exact}} \notin C^3[0, 1].$$

Nevertheless, the terms required by the governing equation, including $u''(x)$ and ${}^{C}D^{3/4}u(x)$, remain well defined.

3. Shifted Chebyshev spectral methods

3.1. Shifted Chebyshev polynomials

The shifted Chebyshev polynomials are obtained from the classical Chebyshev polynomials by mapping the interval $[0, L]$ into $[-1, 1]$. The shifted Chebyshev polynomial is defined by Mason and Handscomb [16] and Canuto et al. [17]

$$T_{L,n}(x) = T_n\left(\frac{2x}{L} - 1\right), \qquad 0 \le x \le L, \tag{8}$$

where $T_n(\cdot)$ is the classical Chebyshev polynomial of degree n.

Using N unknown coefficients, the approximate solution is represented in terms of the shifted Chebyshev polynomial basis as

$$u_N(x) = \sum_{n=0}^{N-1} c_n\, T_{L,n}(x) = C^T \Phi_N(x), \tag{9}$$

where

$$C^T = [c_0, c_1, \ldots, c_{N-1}], \qquad \Phi_N(x) = \begin{bmatrix} T_{L,0}(x) \\ T_{L,1}(x) \\ \vdots \\ T_{L,N-1}(x) \end{bmatrix}. \tag{10}$$

Using the operational matrix of fractional differentiation, we write

$${}^{C}D^{\alpha}\Phi_N(x) \simeq D_N^{(\alpha)}\Phi_N(x), \tag{11}$$

where $D_N^{(\alpha)}$ denotes the corresponding finite-dimensional operational representation.

To clarify the construction of $D_N^{(\alpha)}$, each shifted Chebyshev polynomial is first expressed in monomial form:

$$T_{L,n}(x) = \sum_{r=0}^{n} a_{n,r} x^r, \qquad n = 0, 1, \ldots, N-1, \tag{12}$$

where the coefficients $a_{n,r}$ follow from the transformation in Equation (8). Applying the Caputo power rule term by term gives

$${}^{C}D^{\alpha}T_{L,n}(x) = \sum_{r=\lceil\alpha\rceil}^{n} a_{n,r} \frac{\Gamma(r+1)}{\Gamma(r-\alpha+1)} x^{r-\alpha}. \tag{13}$$

The resulting fractional derivatives are represented in the selected finite approximation space to form the entries of $D_N^{(\alpha)}$. In the Tau formulation, these expressions enter the weighted projection equations. In the collocation formulation, they are evaluated directly at the selected nodes. The approximation sign in Equation (11) therefore reflects the truncation of the finite-dimensional representation [8,9,12,18].

The shifted Chebyshev approximation framework is summarized by Equations (9)–(11). The initial or boundary conditions are then incorporated into the formulation. Consequently, the original fractional differential equation is reduced to a finite system of algebraic equations for the coefficient vector C.

The Shifted Chebyshev Tau Method uses a global polynomial representation together with weighted residual conditions. For the smooth benchmark solutions considered in this study, the method produces very small numerical errors at the selected approximation orders. Its implementation, however, requires the evaluation of projection integrals when forming the algebraic system.

3.2. Shifted Chebyshev Collocation Method

As in the Tau method, the Shifted Chebyshev Collocation Method starts with an approximation of the solution in the form

$$u_N(x) = \sum_{n=0}^{N-1} c_n \, T_{L,n}(x). \tag{14}$$

Suppose that m equations are reserved for the prescribed initial or boundary conditions. Since the approximation in Equation (14) contains N unknown coefficients,

the number of residual collocation equations is

$$n_c = N - m.$$

In the collocation approach, instead of imposing weighted residual conditions as in the Tau formulation, the residual is forced to vanish at the selected collocation points. Consequently,

$$R_N(x_i) = 0, \qquad i = 1, 2, \ldots, n_c. \tag{15}$$

For computational convenience, the collocation points are chosen as the shifted Chebyshev–Gauss points in $[0, L]$:

$$x_i = \frac{L}{2}\left[1 + \cos\left(\frac{(2i-1)\pi}{2n_c}\right)\right], \qquad i = 1, 2, \ldots, n_c. \tag{16}$$

The nonuniform distribution of these points places more nodes near the endpoints of the interval. This reduces the interpolation difficulties that may arise with equally spaced points and is appropriate for global polynomial collocation. For sufficiently regular solutions, shifted Chebyshev approximations may exhibit high-order or spectral convergence. When the solution has reduced regularity, the observed convergence generally becomes algebraic [5,16,17].

The algebraic system is obtained by evaluating the residual at the collocation nodes; that is, by enforcing Equation (15) at the points (16), together with the m prescribed initial or boundary conditions.

Theorem 1 (Exact polynomial reproduction)**.** *Consider a linear fractional differential problem whose exact solution* u_{exact} *belongs to the shifted Chebyshev approximation space*

$$\mathbb{P}_{N-1} = \text{span}\left\{T_{L,0}, T_{L,1}, \ldots, T_{L,N-1}\right\}.$$

Assume that the fractional derivative terms are evaluated exactly for the basis representation and that the resulting SCTM or SCCM algebraic system is nonsingular. Then, in exact arithmetic, the corresponding shifted Chebyshev method recovers u_{exact} *exactly.*

Proof. Since $u_{\text{exact}} \in \mathbb{P}_{N-1}$, there exists a coefficient vector C_{exact} such that

$$u_{\text{exact}}(x) = C_{\text{exact}}^T \Phi_N(x).$$

Direct substitution of this representation into the governing equation gives an identically zero residual, and the prescribed initial or boundary conditions are satisfied. Therefore, C_{exact} satisfies all weighted residual equations in SCTM and all nodal residual equations in SCCM. The assumed nonsingularity of the discrete system implies uniqueness of its coefficient vector. Hence, the computed coefficient vector is C_{exact}, and the exact polynomial solution is recovered. □

Theorem 1 explains the precision-level errors obtained by SCTM and SCCM in the polynomial benchmark problems whenever the exact solution belongs to the selected

approximation space.

4. Haar Wavelet Collocation Method

Haar wavelets form an orthogonal basis of piecewise-constant functions on $[0,1]$ [23,24]. The corresponding scaling function is defined by

$$h_0(t) = 1, \qquad 0 \le t < 1. \tag{17}$$

The mother wavelet is given by

$$h_1(t) = \begin{cases} 1, & 0 \le t < \dfrac{1}{2}, \\ -1, & \dfrac{1}{2} \le t < 1. \end{cases} \tag{18}$$

More generally, for $j \ge 0$, $k = 0, 1, \ldots, 2^j - 1$, and $i = 2^j + k$, the Haar function is defined by

$$h_i(t) = \begin{cases} 1, & \dfrac{k}{2^j} \le t < \dfrac{k+\frac{1}{2}}{2^j}, \\ -1, & \dfrac{k+\frac{1}{2}}{2^j} \le t < \dfrac{k+1}{2^j}, \\ 0, & \text{otherwise.} \end{cases} \tag{19}$$

For $m = 2^J$, define the Haar basis vector by

$$H_m(t) = \begin{bmatrix} h_0(t) & h_1(t) & \cdots & h_{m-1}(t) \end{bmatrix}^T. \tag{20}$$

A function $f(t)$ can be approximated by

$$f(t) \simeq \sum_{i=0}^{m-1} a_i h_i(t) = A^T H_m(t). \tag{21}$$

Depending on the governing equation, either the highest required integer derivative or a selected Caputo derivative is expanded in the Haar basis. For a Caputo derivative of order α, this representation is written as

$${}^C D^\alpha u(t) \simeq K_m^T H_m(t). \tag{22}$$

To follow the conventional Haar operational-matrix notation, I^α denotes in this section the same left-sided Riemann–Liouville fractional integral represented by J^α in Equation (1). Fractional integration is represented through the operational matrix

$$I^\alpha H_m(t) \simeq P_m^\alpha H_m(t). \tag{23}$$

To describe the construction of P_m^α, let

$$t_\ell = \frac{2\ell - 1}{2m}, \qquad \ell = 1, 2, \ldots, m,$$

be the Haar midpoint collocation points, and define

$$\mathcal{H}_m = \begin{bmatrix} H_m(t_1) & H_m(t_2) & \cdots & H_m(t_m) \end{bmatrix}. \tag{24}$$

For every Haar basis function,

$$I^\alpha h_i(t) = \frac{1}{\Gamma(\alpha)} \int_0^t (t-s)^{\alpha-1} h_i(s)\, ds. \tag{25}$$

Let

$$\mathcal{I}_m^{(\alpha)} = \begin{bmatrix} I^\alpha H_m(t_1) & I^\alpha H_m(t_2) & \cdots & I^\alpha H_m(t_m) \end{bmatrix}. \tag{26}$$

Enforcing Equation (23) at the midpoint collocation points gives

$$\mathcal{I}_m^{(\alpha)} \simeq P_m^\alpha \mathcal{H}_m.$$

Since the Haar evaluation matrix $\mathcal{H}_m$ is nonsingular at the midpoint grid, the fractional integration matrix is constructed as

$$P_m^\alpha = \mathcal{I}_m^{(\alpha)} \mathcal{H}_m^{-1}. \tag{27}$$

If $n-1 < \alpha \leq n$, the relation between the Caputo derivative and the corresponding fractional integral gives the general reconstruction

$$u_m(t) \simeq K_m^T P_m^\alpha H_m(t) + \sum_{r=0}^{n-1} \frac{u^{(r)}(0)}{r!} t^r. \tag{28}$$

The Haar operational-matrix construction and its applications to fractional differential equations are discussed in the literature [25–28]. Relevant error and convergence analyses are provided in the study by Chen et al. [39] and Majak et al. [40].

In the numerical implementations, appropriate endpoint correction terms are also included so that the prescribed initial conditions are satisfied independently of the unknown Haar coefficients. The corrected reconstruction corresponding to each governing equation is given explicitly in the numerical examples.

5. Numerical algorithm

For each numerical method, the following steps are applied:

(1) Approximate the solution using the selected basis functions.
(2) Construct the corresponding operational-matrix formulation.
(3) Substitute the approximation into the fractional differential equation.
(4) Generate the residual function.
(5) Apply Tau projection, shifted Chebyshev collocation, or Haar midpoint collocation.
(6) Incorporate the prescribed initial or boundary conditions.
(7) Solve the resulting algebraic system.
(8) Compare the numerical and exact solutions.

Computational cost

For a balanced approximation containing N unknown coefficients, each method produces an $N \times N$ algebraic system. When a general dense direct solver is used, the solution stage requires $O(N^3)$ arithmetic operations and $O(N^2)$ memory.

The main computational difference among the three methods arises during matrix assembly. In SCTM, the matrix entries are obtained from weighted projection equations. Approximately $O(N^2)$ weighted integrals must therefore be evaluated, and the actual cost of these integrations depends on whether symbolic integration or numerical quadrature is used.

SCCM replaces the projection integrals by residual and basis evaluations at the collocation nodes. Its assembly consequently requires approximately $O(N^2)$ function and operator evaluations.

For HWCM, the construction of a fractional integration matrix through Equation (27) involves matrices of order N. A direct matrix inversion or factorization has a cost of $O(N^3)$. However, the resulting operational matrices can be reused for problems having the same fractional orders and approximation size. Once they have been constructed, the problem-dependent Haar system is assembled using approximately $O(N^2)$ matrix-entry evaluations.

These operation counts describe the general algorithmic costs. The measured CPU times reported in the numerical examples are implementation-dependent and also reflect symbolic manipulation, working precision, software, and hardware.

6. Methodology

All computations were performed using Wolfram Mathematica 13.2. Separate computational routines were developed for the Shifted Chebyshev Tau Method (SCTM), the Shifted Chebyshev Collocation Method (SCCM), and the Haar Wavelet Collocation Method (HWCM).

For each benchmark problem, the corresponding basis functions and operational matrices were first constructed. The resulting algebraic system associated with each numerical method was then solved independently to determine the unknown expansion coefficients. These coefficients were subsequently used to evaluate the numerical solution over the computational interval.

A balanced comparison was performed using

$$N \in \{4, 8, 16, 32\}, \tag{29}$$

where every method uses exactly N unknown coefficients and N algebraic equations. The principal numerical results are reported at

$$N = 32.$$

Throughout the text and numerical tables, N denotes the number of unknown coefficients used by each method. In the computational figures, the symbol q denotes

the same balanced approximation size. Thus, the notation used in the figures satisfies

$$q = N.$$

All computations were carried out using a working precision of 60 decimal digits. The implementations of SCTM and SCCM were independently verified using separate computational routines. Whenever an exact polynomial solution belongs to the selected shifted Chebyshev approximation space, both methods reproduce that solution up to the adopted working-precision threshold, in agreement with Theorem 1. Consequently, their reported maximum and RMS error values coincide within the displayed numerical precision in those cases. This agreement is therefore a genuine numerical result rather than a computational or transcription error.

The numerical approximations were evaluated independently on a common test grid containing

$$M = 2,001$$

equally spaced points over

$$0 \le x \le 1 - 10^{-12}.$$

This grid was not used in the assembly or solution of any of the three algebraic systems. Its use therefore provides an independent assessment of the computed approximations.

The maximum absolute error and the root mean square error were computed, respectively, as

$$E_{\max} = \max_{1 \le i \le M} \left| u_{\text{exact}}(x_i) - u_N(x_i) \right|, \tag{30}$$

and

$$E_{\text{RMS}} = \left[\frac{1}{M} \sum_{i=1}^{M} \left| u_{\text{exact}}(x_i) - u_N(x_i) \right|^2 \right]^{1/2}. \tag{31}$$

The maximum differential-equation residual was also evaluated on the same independent grid. For the prescribed initial conditions, the corresponding residuals were computed directly at the initial point.

For two successive balanced levels $N/2$ and N, the observed maximum-error convergence rate was calculated from

$$p_N = \frac{\log \left[E_{\max}(N/2) / E_{\max}(N) \right]}{\log 2}. \tag{32}$$

Equation (32) is applied only when both successive errors are strictly positive and remain above the adopted working-precision threshold. A conventional observed rate is not reported when the corresponding exact polynomial solution is reproduced to numerical precision.

The coefficient matrices were examined through their spectral two-norm condition numbers, row-scaled condition numbers, numerical ranks, and matrix densities. Assembly time, linear-system solution time, and total computational time were recorded separately. All timings were obtained within the same Mathematica session and are used as relative implementation-cost indicators rather than machine-independent complexity

measures.

All numerical tables, two-dimensional comparisons, and three-dimensional graphical illustrations presented in this paper were generated directly from the computed numerical data using the built-in plotting functions of Wolfram Mathematica 13.2.

7. Applications and computational results

7.1. Example 1

This example considers a simple initial value problem for a fractional differential equation. Such problems occur in models of dynamical systems with memory, where the present state depends on the history of the process. From a numerical point of view, the problem is useful for examining how the three numerical formulations reproduce a known smooth polynomial solution under balanced approximation settings. Its simple structure makes it a suitable benchmark for verifying the implementations, studying convergence, and comparing the resulting algebraic systems.

Consider

$$ {}^{C}D^{3/2}u(x) + u(x) = x^2 - x + \frac{4}{\sqrt{\pi}}\sqrt{x}, \qquad 0 \le x \le 1, \tag{33} $$

subject to

$$ u(0) = 0, \qquad u'(0) = -1. \tag{34} $$

The exact solution is

$$ u_{\text{exact}}(x) = x^2 - x. \tag{35} $$

Direct substitution of Equation (35) into Equation (33) gives an identically zero differential-equation residual, and both initial conditions in Equation (34) are satisfied exactly.

Shifted Chebyshev Tau Method

Using N unknown coefficients, let

$$ u_N(x) = \sum_{i=0}^{N-1} c_i\, T_{L,i}(x), \qquad L = 1. \tag{36} $$

The residual is

$$ R_N(x) = {}^{C}D^{3/2}u_N(x) + u_N(x) - \left(x^2 - x + \frac{4}{\sqrt{\pi}}\sqrt{x} \right). \tag{37} $$

Since two equations are reserved for the initial conditions, the $N-2$ Tau equations are

$$ \int_0^1 R_N(x) T_{L,j}(x) w_L(x)\, dx = 0, \qquad j = 0, 1, \ldots, N-3, \tag{38} $$

where

$$ w_L(x) = \frac{1}{\sqrt{x(L-x)}}, \qquad L = 1, $$

is the shifted Chebyshev weight function. The remaining two equations are obtained

from

$$u_N(0) = 0, \qquad u'_N(0) = -1.$$

Shifted Chebyshev Collocation Method

The Shifted Chebyshev Collocation Method uses the same approximation (36). The residual is imposed at $N-2$ shifted Chebyshev–Gauss points:

$$R_N(x_k) = 0, \qquad k = 1, 2, \ldots, N-2, \tag{39}$$

where

$$x_k = \frac{1}{2}\left[1 + \cos\left(\frac{(2k-1)\pi}{2(N-2)}\right)\right]. \tag{40}$$

Together with the two initial conditions, these equations produce a square system of N equations for the N unknown coefficients.

Haar Wavelet Collocation Method

For the Haar formulation, the Caputo derivative is approximated by

$$^{C}D^{3/2}u(x) \simeq K_N^T H_N(x), \tag{41}$$

where $H_N(x)$ is the vector of the first N Haar basis functions and K_N is the vector of unknown Haar coefficients.

Let $P_N^{1/2}$ and $P_N^{3/2}$ denote the Haar operational matrices of fractional integration of orders $1/2$ and $3/2$, respectively. To enforce both initial conditions directly, the corrected reconstruction is written as

$$u_N(x) = K_N^T\left[P_N^{3/2}H_N(x) - P_N^{3/2}H_N(0) - xP_N^{1/2}H_N(0)\right] - x. \tag{42}$$

Its first derivative is represented by

$$u'_N(x) = K_N^T\left[P_N^{1/2}H_N(x) - P_N^{1/2}H_N(0)\right] - 1. \tag{43}$$

Equations (42) and (43) give

$$u_N(0) = 0, \qquad u'_N(0) = -1$$

independently of the values of the unknown coefficients.

The Haar midpoint collocation points are

$$x_i = \frac{2i-1}{2N}, \qquad i = 1, 2, \ldots, N. \tag{44}$$

Substitution into the governing equation gives

$$\begin{aligned} K_N^T\Big[&H_N(x_i) + P_N^{3/2}H_N(x_i) - P_N^{3/2}H_N(0) \\ &- x_i\, P_N^{1/2}H_N(0)\Big] = x_i^2 + \frac{4}{\sqrt{\pi}}\sqrt{x_i}, \qquad i = 1, 2, \ldots, N. \end{aligned} \tag{45}$$

This produces a square system of N equations for the N components of K_N.

Computational setting and exact-polynomial reproduction

The common computational settings described in Section 6 were used. In particular, the balanced levels were

$$N \in \{4, 8, 16, 32\},$$

and the principal results were obtained at $N = 32$.

The exact solution (35) is a polynomial of degree two. It therefore belongs to the shifted Chebyshev space $\mathbb{P}_{N-1}$ at every balanced level considered here. By Theorem 1, SCTM and SCCM recover the same exact polynomial solution in exact arithmetic. Their reported differences are consequently limited to the adopted working precision.

Numerical solution comparison

Figure 1 compares the exact solution with the three numerical approximations at the principal balanced level $N = 32$.

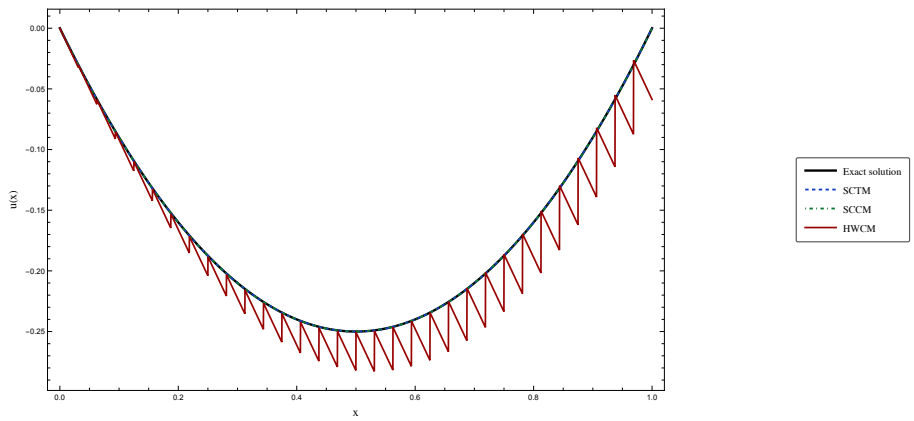

Figure 1. Comparison of the exact and numerical solutions for Example 1 at the principal balanced level $N = 32$.

The SCTM and SCCM curves are indistinguishable from the exact parabolic profile throughout the computational interval. The corrected HWCM approximation preserves the same global shape but displays a visible piecewise sawtooth structure associated with the localized Haar representation. Its deviations become more pronounced toward the right endpoint.

The principal accuracy and residual measures are reported in **Table 1**.

Table 1. Accuracy and residual measures for Example 1 at $N = 32$.

Method	Maximum error	RMS error	Maximum PDE residual	Maximum IC residual
Shifted Chebyshev Tau Method	0^*	0^*	0^*	0^*
Shifted Chebyshev Collocation Method	0^*	0^*	0^*	0^*
Haar Wavelet Collocation Method	5.86881×10^{-2}	2.07534×10^{-2}	2.82927×10^{-1}	0^*

Note: *Numerically zero at the adopted working precision.

At $N = 32$, SCTM and SCCM reproduce the exact polynomial solution to the adopted numerical precision. The corrected HWCM approximation has a maximum absolute error of 5.86881×10^{-2} and an RMS error of 2.07534×10^{-2}. Its maximum

error is attained near $x = 1$. The initial-condition residuals remain numerically zero for all three methods.

Table 2 reports the corresponding matrix and timing diagnostics. The condition numbers are the spectral two-norm condition numbers obtained from the singular values of the coefficient matrices. Row-scaled values are also included to distinguish the effect of row magnitude from the underlying conditioning.

Table 2. Matrix and computational diagnostics for Example 1 at $N = 32$.

Method	$\kappa_2(A)$	Row-scaled $\kappa_2(A)$	Matrix density	Assembly time (s)	Solve time (s)	Total time (s)
Shifted Chebyshev Tau Method	3.46237×10^4	2.16552×10^4	0.942383	4.80578	5.31×10^{-4}	4.80631
Shifted Chebyshev Collocation Method	7.81378×10^4	1.41526×10^4	0.999023	1.605×10^{-2}	4.93×10^{-4}	1.6543×10^{-2}
Haar Wavelet Collocation Method	5.03740	5.26187	0.593750	3.2471×10^{-2}	5.45×10^{-4}	3.3016×10^{-2}

The linear-system solution times are of the same order for the three methods. The principal difference occurs during matrix assembly. SCTM requires weighted projection integrals and consequently has the largest assembly time in this implementation. SCCM avoids these integrals and gives the shortest total time. HWCM has an intermediate total time, while its matrix is considerably better conditioned and less dense than the two Chebyshev matrices.

The reported times were obtained within the same Mathematica session and are used as relative implementation-cost indicators rather than machine-independent complexity measures.

Balanced convergence

The HWCM convergence history is summarized in **Table 3**. The observed maximum-error rate between two successive levels is computed from

$$r_N = \frac{\log[E_{\max}(N/2)/E_{\max}(N)]}{\log 2}. \tag{46}$$

Table 3. Balanced convergence results for HWCM in Example 1.

N	Maximum error	RMS error	Observed rate
4	4.90450×10^{-1}	1.89451×10^{-1}	–
8	2.37709×10^{-1}	8.69375×10^{-2}	1.04491
16	1.17686×10^{-1}	4.20782×10^{-2}	1.01425
32	5.86881×10^{-2}	2.07534×10^{-2}	1.00381

Figure 2 presents the corresponding balanced comparison.

The HWCM maximum error decreases by approximately one half whenever N is doubled. The observed rates approach one, indicating approximately first-order convergence for this formulation. A conventional convergence rate is not reported for SCTM and SCCM because the quadratic exact solution is already contained in their approximation spaces and is reproduced to the adopted precision at every balanced level.

Absolute-error distribution

Figure 3 shows the pointwise absolute-error distributions at $N = 32$ on a logarithmic vertical scale.

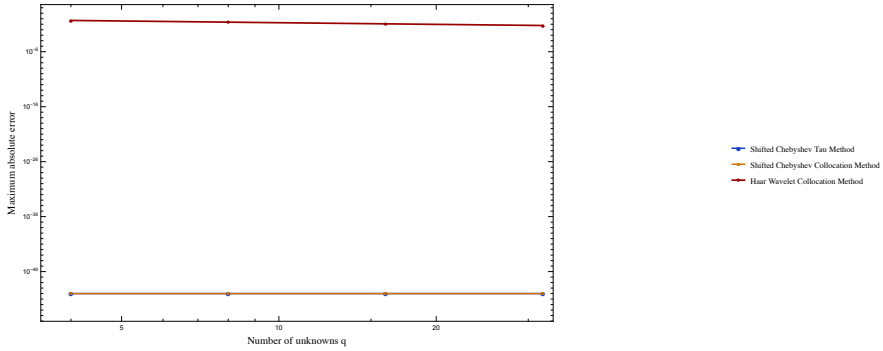

Figure 2. Balanced maximum-error comparison for Example 1 using $N = 4, 8, 16$, and 32 unknowns for every method.

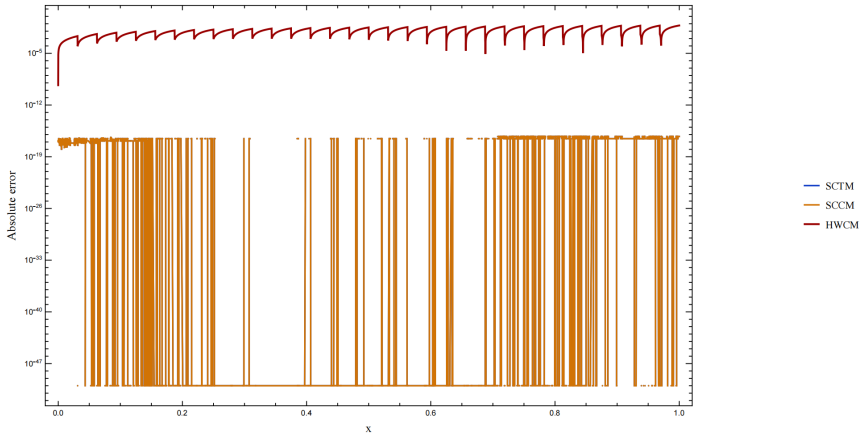

Figure 3. Pointwise absolute-error distributions for Example 1 at $N = 32$.

The SCTM and SCCM errors remain at the numerical-precision floor over the interval. The HWCM error displays a repeated local pattern induced by the piecewise Haar basis. Its envelope generally increases toward the right endpoint, where the maximum error is observed.

Three-dimensional error surfaces

The variation of the pointwise errors with both the spatial coordinate and the balanced approximation size is displayed in **Figure 4**.

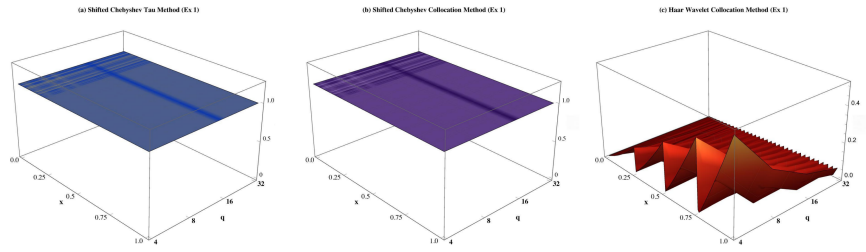

Figure 4. Three-dimensional absolute-error surfaces for Example 1. The HWCM panel shows the actual absolute errors. Since the SCTM and SCCM errors are numerically zero at the adopted working precision, their panels are displayed at a visualization level of 10^{-40} only to make the precision-level surfaces visible. This graphical scaling does not modify the numerical results reported in the tables.

The HWCM surface decreases systematically as N increases, in agreement with the approximately first-order rates in **Table 3**. Its localized peaks reflect the piecewise structure visible in the solution and error plots. In contrast, the SCTM and SCCM panels represent only numerical precision-level plateaus and should not be interpreted as physical error surfaces of order one.

Overall, Example 1 confirms the higher accuracy of the two shifted Chebyshev formulations for this smooth polynomial solution. At the same time, the corrected HWCM formulation satisfies the prescribed initial conditions exactly, converges regularly under balanced refinement, and produces a substantially better-conditioned and less dense algebraic system.

7.2. Example 2

The second benchmark considers a multi-term fractional differential equation involving derivatives of orders 2, $3/2$, 1, and $1/2$. The presence of several derivative terms makes the problem suitable for examining how the three numerical formulations handle multiple operators within the same equation. Since the exact solution is known, the computed approximations can be assessed directly using the maximum absolute error, the root mean square error, the observed convergence behavior, and the properties of the resulting algebraic systems.

Consider

$$u''(x) + {}^{C}D^{3/2}u(x) + u'(x) + {}^{C}D^{1/2}u(x) + u(x) = g(x), \qquad 0 \le x \le 1, \quad (47)$$

where

$$g(x) = 1 - \frac{x^2}{2} - x - \frac{2}{\sqrt{\pi}}\sqrt{x} - \frac{4}{3\sqrt{\pi}}x^{3/2}. \quad (48)$$

The initial conditions are

$$u(0) = 2, \qquad u'(0) = 0. \quad (49)$$

The exact solution is

$$u_{\text{exact}}(x) = 2 - \frac{x^2}{2}. \quad (50)$$

Direct symbolic substitution of Equation (50) into Equation (47) gives a zero differential-equation residual, and the two initial-condition residuals are also exactly zero.

Shifted Chebyshev Tau Method

Using N unknown coefficients, the approximate solution is written as

$$u_N(x) = \sum_{n=0}^{N-1} c_n T_{L,n}(x), \qquad L = 1. \quad (51)$$

The residual is

$$\begin{aligned} R_N(x) = {} & u_N''(x) + {}^{C}D^{3/2}u_N(x) + u_N'(x) + {}^{C}D^{1/2}u_N(x) \\ & + u_N(x) - g(x). \end{aligned} \quad (52)$$

Since two equations are reserved for the initial conditions, the $N-2$ Tau projection equations are

$$\int_0^1 R_N(x)T_{L,j}(x)w_L(x)\,dx = 0, \qquad j = 0, 1, \ldots, N-3. \tag{53}$$

The remaining two equations are obtained from

$$u_N(0) = 2, \qquad u'_N(0) = 0. \tag{54}$$

Shifted Chebyshev Collocation Method

The Shifted Chebyshev Collocation Method uses the same approximation (51). The residual is imposed at $N-2$ shifted Chebyshev–Gauss points:

$$R_N(x_k) = 0, \qquad k = 1, 2, \ldots, N-2, \tag{55}$$

where

$$x_k = \frac{1}{2}\left[1 + \cos\left(\frac{(2k-1)\pi}{2(N-2)}\right)\right]. \tag{56}$$

Together with the two initial conditions in Equation (54), these equations produce a square system of N equations for the N unknown coefficients.

Haar Wavelet Collocation Method

For the Haar formulation, the highest-order derivative is approximated by

$$u''_N(x) \simeq K_N^T H_N(x), \tag{57}$$

where $H_N(x)$ denotes the vector of the first N Haar basis functions and K_N is the vector of unknown coefficients.

Let P_N^α denote the Haar operational matrix of fractional integration of order α, and define

$$p_\alpha^0 = P_N^\alpha H_N(0). \tag{58}$$

The corrected reconstruction of the first derivative is

$$u'_N(x) = K_N^T\left[P_N^1 H_N(x) - p_1^0\right]. \tag{59}$$

The Caputo derivative of order $3/2$ is represented by

$${}^C D^{3/2}u_N(x) = K_N^T\left[P_N^{1/2}H_N(x) - p_{1/2}^0\right]. \tag{60}$$

The Caputo derivative of order $1/2$ is represented by

$${}^C D^{1/2}u_N(x) = K_N^T\left[P_N^{3/2}H_N(x) - p_{3/2}^0 - \frac{x^{1/2}}{\Gamma(3/2)}p_1^0\right]. \tag{61}$$

The approximate solution is reconstructed as

$$u_N(x) = K_N^T\left[P_N^2 H_N(x) - p_2^0 - xp_1^0\right] + 2. \tag{62}$$

Equations (59) and (62) ensure that

$$u_N(0) = 2, \qquad u'_N(0) = 0$$

independently of the unknown coefficient values.

The Haar midpoint collocation points are

$$x_i = \frac{2i-1}{2N}, \qquad i = 1, 2, \ldots, N. \tag{63}$$

Substitution into Equation (47) gives

$$K_N^T \mathcal{B}_N(x_i) = g(x_i) - 2, \qquad i = 1, 2, \ldots, N, \tag{64}$$

where

$$\begin{aligned} \mathcal{B}_N(x) = H_N(x) &+ \left[P_N^{1/2} H_N(x) - p_{1/2}^0\right] \\ &+ \left[P_N^1 H_N(x) - p_1^0\right] \\ &+ \left[P_N^{3/2} H_N(x) - p_{3/2}^0 - \frac{x^{1/2}}{\Gamma(3/2)} p_1^0\right] \\ &+ \left[P_N^2 H_N(x) - p_2^0 - x p_1^0\right]. \end{aligned} \tag{65}$$

This formulation produces a square system containing N equations and N unknown Haar coefficients.

Computational setting and exact-polynomial reproduction

The common computational settings described in Section 6 were used. The principal results were obtained at $N = 32$.

The exact solution (50) is a quadratic polynomial and therefore belongs to every shifted Chebyshev approximation space used in the balanced study. By Theorem 1, both SCTM and SCCM reproduce the exact solution to the adopted numerical precision. Their nearly identical accuracy is therefore a consequence of polynomial exactness rather than an accidental numerical agreement.

Numerical solution comparison

Figure 5 compares the exact and numerical solutions at the principal balanced level $N = 32$.

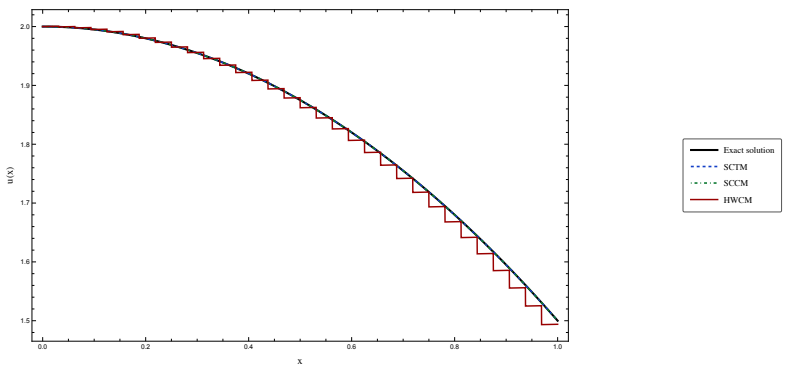

Figure 5. Comparison of the exact and numerical solutions for Example 2 at the principal balanced level $N = 32$.

The SCTM and SCCM approximations are visually indistinguishable from the exact decreasing quadratic profile. The corrected HWCM approximation follows the same global behavior but exhibits a visible piecewise staircase structure. The deviations generally increase toward the upper end of the interval.

The principal error and residual measures are summarized in **Table 4**.

Table 4. Accuracy and residual measures for Example 2 at $N = 32$.

Method	Maximum error	RMS error	x at maximum error	Maximum PDE residual	Maximum IC residual
Shifted Chebyshev Tau Method	0^*	0^*	–	0^*	0^*
Shifted Chebyshev Collocation Method	0^*	0^*	–	0^*	0^*
Haar Wavelet Collocation Method	3.71425×10^{-2}	1.11536×10^{-2}	0.969000	1.61106×10^{-1}	0^*

Note: *Numerically zero at the adopted working precision. The symbol "–" indicates that the location of the maximum is not uniquely defined because the error is numerically zero throughout the test grid.

At $N = 32$, SCTM and SCCM reproduce the quadratic exact solution to the adopted numerical precision. The corrected HWCM approximation has a maximum absolute error of 3.71425×10^{-2} and an RMS error of 1.11536×10^{-2}. Its maximum error occurs near $x = 0.969$, while both prescribed initial conditions are satisfied to the adopted precision.

The matrix and timing diagnostics are given in **Table 5**.

Table 5. Matrix and computational diagnostics for Example 2 at $N = 32$.

Method	$\kappa_2(A)$	Row-scaled $\kappa_2(A)$	Matrix density	Assembly time (s)	Solve time (s)	Total time (s)
Shifted Chebyshev Tau Method	8.46790×10^5	7.72694×10^4	0.970703	3.98980×10^1	5.40×10^{-4}	3.98986×10^1
Shifted Chebyshev Collocation Method	2.09115×10^6	6.87303×10^3	0.999023	2.5047×10^{-2}	5.71×10^{-4}	2.5618×10^{-2}
Haar Wavelet Collocation Method	1.03747×10^1	1.22200×10^1	0.593750	4.5115×10^{-2}	5.28×10^{-4}	4.5643×10^{-2}

The linear-system solution times are nearly identical because all three systems have size 32×32. The principal timing difference occurs during matrix construction. SCTM requires weighted projection integrals and therefore has the largest assembly time in the present implementation. SCCM gives the smallest total time, whereas HWCM requires slightly more assembly time than SCCM but produces a much better-conditioned and less dense coefficient matrix.

The reported CPU times are implementation-dependent and are used only as relative indicators obtained within the same Mathematica session.

Balanced convergence

The balanced HWCM convergence history is given in **Table 6**. The observed maximum-error rate is calculated from

$$r_N = \frac{\log[E_{\max}(N/2)/E_{\max}(N)]}{\log 2}. \tag{66}$$

Table 6. Balanced convergence results for HWCM in Example 2.

N	Maximum error	RMS error	Observed rate
4	1.46424×10^{-1}	6.57407×10^{-2}	–
8	8.60965×10^{-2}	2.67784×10^{-2}	0.766127
16	5.65997×10^{-2}	1.57214×10^{-2}	0.605161
32	3.71425×10^{-2}	1.11536×10^{-2}	0.607724

Figure 6 shows the corresponding balanced comparison.

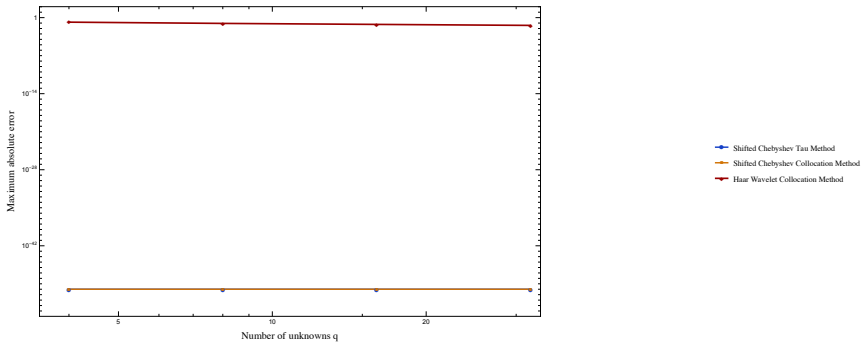

Figure 6. Balanced maximum-error comparison for Example 2 using $N = 4, 8, 16$, and 32 unknowns for every method.

The HWCM maximum error decreases monotonically under refinement. The last two observed rates are approximately 0.61, indicating sublinear algebraic convergence for this multi-term problem. A conventional convergence rate is not reported for SCTM and SCCM because the quadratic exact solution is already contained in their approximation spaces and is reproduced to the adopted precision at every balanced level.

Absolute-error distribution

Figure 7 presents the pointwise absolute-error distributions at the principal level $N = 32$.

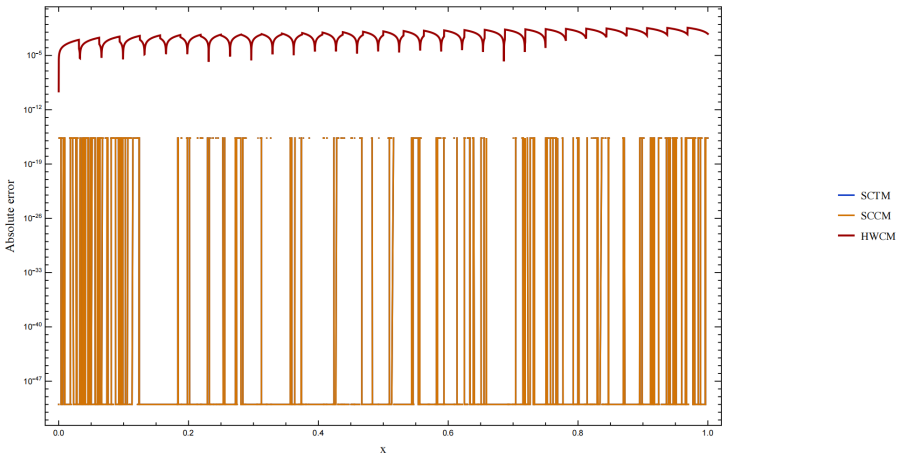

Figure 7. Pointwise absolute-error distributions for Example 2 at $N = 32$.

The SCTM and SCCM errors remain at the numerical-precision floor over the computational interval. The HWCM error exhibits a repeated local pattern associated with the piecewise Haar basis. Its envelope generally grows toward the right-hand portion of the interval, with the largest error occurring near $x = 0.969$.

Three-dimensional error surfaces

Figure 8 shows the variation of the pointwise errors with both x and the balanced approximation size N.

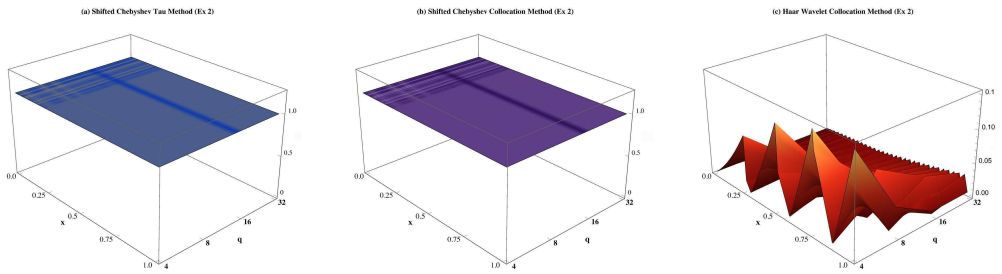

Figure 8. Three-dimensional absolute-error surfaces for Example 2. The HWCM panel shows the actual absolute errors. Since the SCTM and SCCM errors reach the adopted numerical-precision level, their panels are displayed at a visualization level of 10^{-40} only to make the nearly flat surfaces visible. This visualization scaling does not alter the reported numerical errors.

The HWCM surface decreases systematically as N increases, although the reduction is slower than first order. The localized peaks and staircase patterns reflect the piecewise nature of the Haar representation. The SCTM and SCCM surfaces correspond only to precision-level errors and should not be interpreted as errors of order one.

Overall, Example 2 confirms that the shifted Chebyshev formulations provide substantially higher accuracy for the selected smooth quadratic solution. The corrected HWCM formulation satisfies the initial conditions exactly and converges monotonically, while also producing a much better-conditioned and less dense algebraic system.

7.3. Example 3

A further benchmark is given by an initial value problem whose governing equation contains a fractional derivative of order $1/2$. Compared with the preceding cases, the exact solution has a higher polynomial degree and therefore provides a useful setting for examining polynomial reproduction under balanced approximation levels. Since the exact solution is known, the computed approximations can be assessed directly using the maximum absolute error, the root mean square error, and the observed convergence behavior.

Consider the fractional differential equation

$$ {}^{C}D^{1/2}u(x) + u(x) = x^4 - \frac{x^3}{2} - \frac{3x^{5/2}}{\Gamma(7/2)} + \frac{24x^{7/2}}{\Gamma(9/2)}, \qquad 0 \le x \le 1, \tag{67} $$

subject to

$$ u(0) = 0. \tag{68} $$

The exact solution is

$$ u_{\text{exact}}(x) = x^4 - \frac{x^3}{2}. \tag{69} $$

The fractional terms in Equation (67) may equivalently be written as

$$ -\frac{3x^{5/2}}{\Gamma(7/2)} + \frac{24x^{7/2}}{\Gamma(9/2)} = -\frac{8}{5\sqrt{\pi}}x^{5/2} + \frac{128}{35\sqrt{\pi}}x^{7/2}. $$

Direct symbolic substitution of Equation (69) into Equation (67) gives a zero differential-equation residual, while the prescribed initial condition is also satisfied exactly.

Shifted Chebyshev Tau Method

Using N unknown coefficients, the numerical approximation is represented by

$$u_N(x) = \sum_{n=0}^{N-1} c_n \, T_{L,n}(x), \qquad L = 1. \tag{70}$$

The corresponding residual is

$$R_N(x) = {}^{C}D^{1/2}u_N(x) + u_N(x) - \left(x^4 - \frac{x^3}{2} - \frac{3x^{5/2}}{\Gamma(7/2)} + \frac{24x^{7/2}}{\Gamma(9/2)} \right). \tag{71}$$

Since one equation is reserved for the initial condition, the $N-1$ weighted residual equations are

$$\int_0^1 R_N(x) T_{L,j}(x) w_L(x) \, dx = 0, \qquad j = 0, 1, \ldots, N-2. \tag{72}$$

The remaining equation is obtained from

$$u_N(0) = 0. \tag{73}$$

Shifted Chebyshev Collocation Method

The Shifted Chebyshev Collocation Method uses the same approximation (70). The residual is evaluated at $N-1$ shifted Chebyshev–Gauss nodes:

$$R_N(x_k) = 0, \qquad k = 1, 2, \ldots, N-1, \tag{74}$$

where

$$x_k = \frac{1}{2}\left[1 + \cos\left(\frac{(2k-1)\pi}{2(N-1)} \right) \right], \qquad k = 1, 2, \ldots, N-1. \tag{75}$$

Together with $u_N(0) = 0$, these equations produce a square system of N equations for the N unknown coefficients.

Haar Wavelet Collocation Method

For the Haar formulation, the Caputo derivative is approximated by

$${}^{C}D^{1/2}u_N(x) \simeq K_N^T H_N(x), \tag{76}$$

where $H_N(x)$ denotes the vector of the first N Haar basis functions and K_N is the vector of unknown Haar coefficients.

Using the operational matrix $P_N^{1/2}$, the corrected reconstruction of the approximate solution is

$$u_N(x) = K_N^T \left[P_N^{1/2} H_N(x) - P_N^{1/2} H_N(0) \right]. \tag{77}$$

The subtraction of the endpoint vector ensures directly that

$$u_N(0) = 0$$

independently of the unknown coefficients.

Using the Haar midpoint collocation points

$$x_i = \frac{2i-1}{2N}, \qquad i = 1, 2, \ldots, N, \tag{78}$$

the corrected Haar algebraic system becomes

$$K_N^T \left[H_N(x_i) + P_N^{1/2} H_N(x_i) - P_N^{1/2} H_N(0) \right] = g(x_i), \qquad i = 1, 2, \ldots, N, \tag{79}$$

where

$$g(x) = x^4 - \frac{x^3}{2} - \frac{3x^{5/2}}{\Gamma(7/2)} + \frac{24x^{7/2}}{\Gamma(9/2)}. \tag{80}$$

Equation (79) gives a square system containing N equations and N unknown Haar coefficients.

Computational setting and exact-polynomial reproduction

The common computational settings described in Section 6 were used. The balanced approximation sizes were

$$N \in \{4, 8, 16, 32\},$$

and the principal results were obtained at $N = 32$.

The exact solution (69) is a polynomial of degree four. It is not contained in the $N = 4$ shifted Chebyshev approximation space, whose highest polynomial degree is three. For $N \geq 8$, however, the exact solution belongs to the approximation space. Consequently, by Theorem 1, SCTM and SCCM reproduce it to the adopted numerical precision at the three higher balanced levels.

Numerical solution comparison

Figure 9 compares the exact solution with the numerical solutions obtained by SCTM, SCCM, and HWCM at the principal balanced level $N = 32$.

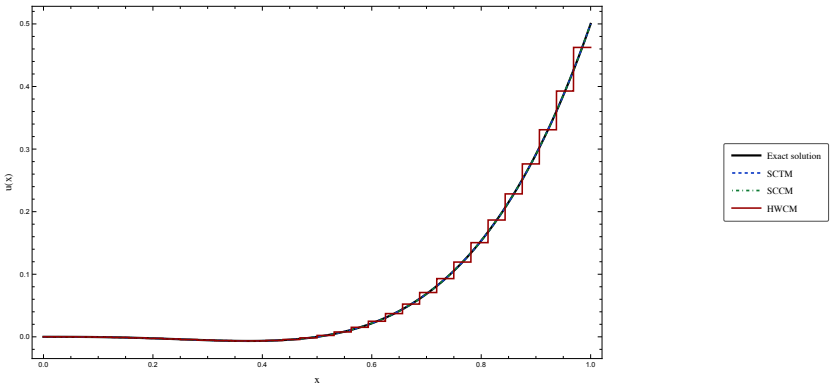

Figure 9. Comparison of the exact and numerical solutions for Example 3 at the principal balanced level $N = 32$.

The SCTM and SCCM curves are visually indistinguishable from the exact solution over the full computational interval. Both methods reproduce the mild variation near the beginning of the interval and the sharper increase as x approaches 1. The corrected HWCM approximation follows the same general profile, although its localized piecewise structure becomes visible in the region where the exact solution increases more rapidly.

The maximum absolute error and the root mean square error at $N = 32$ are listed in **Table 7**.

Table 7. Error summary for Example 3 at $N = 32$.

Method	Maximum error	RMS error
Shifted Chebyshev Tau Method	0^*	0^*
Shifted Chebyshev Collocation Method	0^*	0^*
Haar Wavelet Collocation Method	3.75539×10^{-2}	7.74609×10^{-3}

Note: * Numerically zero at the adopted working precision.

At $N = 32$, SCTM and SCCM reproduce the exact polynomial solution to the adopted numerical precision. Their agreement follows from the inclusion of the degree-four exact solution in the shifted Chebyshev approximation space rather than from an accidental coincidence between the two numerical procedures.

The corrected HWCM approximation gives a maximum error of 3.75539×10^{-2} and an RMS error of 7.74609×10^{-3}. The maximum error occurs near the right endpoint, where the exact solution has its largest magnitude and steepest increase. The maximum differential-equation residual for HWCM is 1.13779×10^{-1}, while its initial-condition residual is numerically zero.

Balanced convergence

The balanced convergence behavior of HWCM is summarized in **Table 8**. The observed maximum-error rate is computed from

$$r_N = \frac{\log[E_{\max}(N/2)/E_{\max}(N)]}{\log 2}. \tag{81}$$

Table 8. Balanced convergence results for HWCM in Example 3.

N	Maximum error	RMS error	Observed rate
4	2.30671×10^{-1}	5.88378×10^{-2}	–
8	1.33824×10^{-1}	3.05807×10^{-2}	0.785495
16	7.22443×10^{-2}	1.54383×10^{-2}	0.889385
32	3.75539×10^{-2}	7.74609×10^{-3}	0.943922

Figure 10 presents the corresponding balanced comparison.

At $N = 4$, SCTM and SCCM give maximum errors of 1.51180×10^{-2} and 2.40608×10^{-2}, respectively, because the degree-four exact solution is not contained in the corresponding degree-three approximation space. At $N = 8$, the exact solution enters the Chebyshev approximation space, and both errors drop to the adopted numerical-precision level.

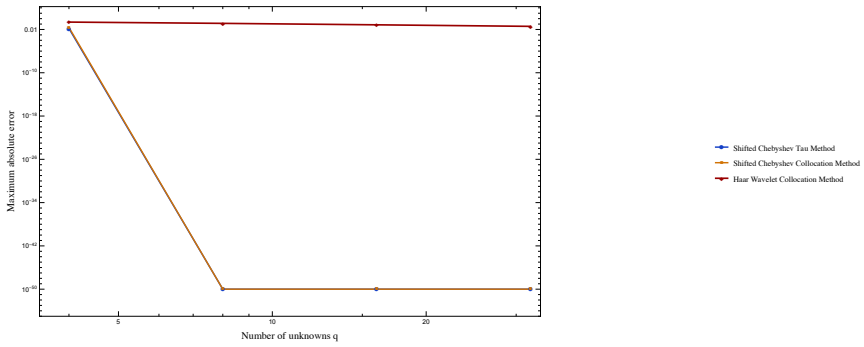

Figure 10. Balanced maximum-error comparison for Example 3 using $N = 4, 8, 16$, and 32 unknowns for every method.

The HWCM error decreases monotonically at every balanced refinement. Its observed rate increases from 0.785495 to 0.943922, showing that its convergence behavior approaches first order as N increases.

Absolute-error distribution

Figure 11 shows the pointwise absolute-error distributions at $N = 32$.

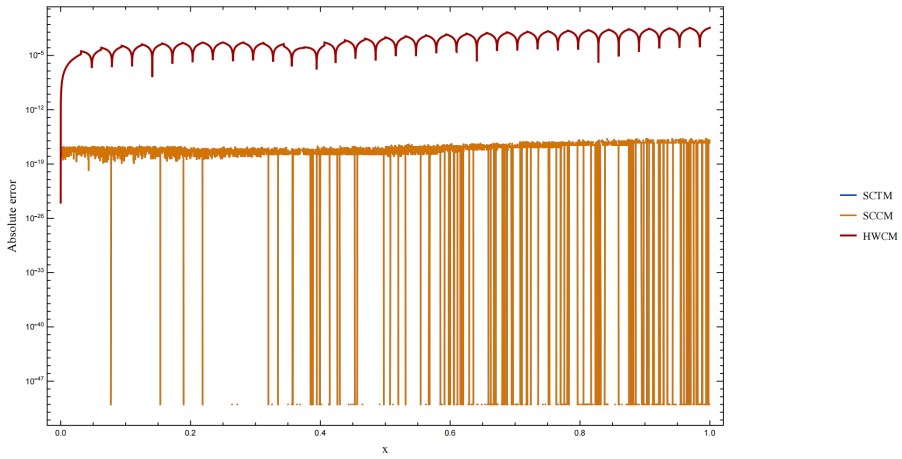

Figure 11. Pointwise absolute-error distributions for Example 3 at $N = 32$.

The SCTM and SCCM errors remain at the adopted numerical-precision level throughout the interval. The HWCM error exhibits a repeated localized pattern associated with the piecewise Haar basis. Its envelope increases gradually toward the right endpoint, where the largest pointwise deviation is observed.

Three-dimensional logarithmic error surfaces

Because the three methods produce errors over widely separated orders of magnitude, the three-dimensional surfaces are displayed using a common logarithmic scale in **Figure 12**.

The SCTM and SCCM surfaces show visible errors at $N = 4$, followed by an abrupt decrease to the precision floor at $N = 8$, 16, and 32. This behavior is consistent with exact polynomial reproduction once the approximation space contains the degree-four solution.

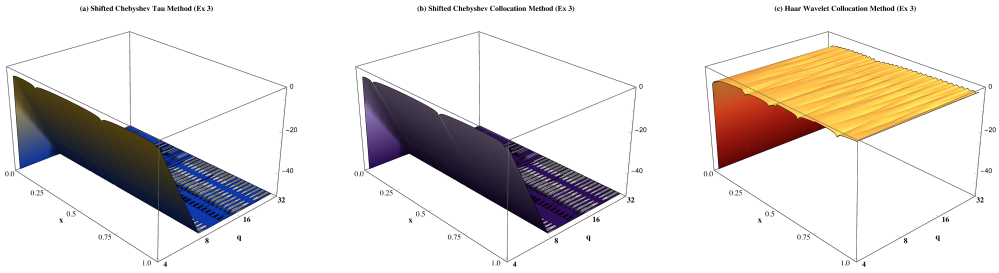

Figure 12. Three-dimensional logarithmic absolute-error surfaces for Example 3. The vertical coordinate represents $\log_{10}\big(\max\{|u_{\text{exact}}(x) - u_N(x)|, 10^{-50}\}\big)$. The floor 10^{-50} is introduced only to display precision-level errors on a finite common logarithmic scale.

The HWCM surface decreases continuously rather than abruptly as the balanced level increases. The repeated ridges reflect the localized piecewise representation, while their declining heights confirm the regular convergence observed in **Table 8**.

The corresponding matrix and computational diagnostics are reported in **Table 9**.

Table 9. Matrix and computational diagnostics for Example 3 at $N = 32$.

Method	$\kappa_2(A)$	**Row-scaled** $\kappa_2(A)$	**Matrix density**	**Total time (s)**
Shifted Chebyshev Tau Method	3.54783×10^1	1.87166×10^1	0.970703	2.15304×10^1
Shifted Chebyshev Collocation Method	8.40856×10^1	7.95499	1.000000	2.1568×10^{-2}
Haar Wavelet Collocation Method	6.32541	6.67284	0.593750	2.2801×10^{-2}

Although the shifted Chebyshev methods provide substantially smaller approximation errors at $N = 32$, the HWCM coefficient matrix is less dense and has the smallest unscaled condition number. SCCM and HWCM have similar total computational times, whereas the weighted projection calculations make SCTM substantially more expensive in the present implementation.

Overall, Example 3 shows that the two shifted Chebyshev formulations recover the smooth degree-four solution to the adopted precision once a sufficiently rich polynomial space is used. The corrected HWCM formulation satisfies the initial condition exactly and approaches first-order convergence under balanced refinement, although its reported errors remain larger than those of SCTM and SCCM.

7.4. Example 4

A linear multi-term fractional differential equation with derivatives of different orders is examined in the fourth test problem. This formulation offers an additional basis for comparing the three numerical methods within the same model. The known exact solution allows the corresponding approximations to be evaluated through the maximum absolute error, the root mean square error, and the observed convergence behavior.

Consider

$$u''(x) + {}^{C}D^{3/4}u(x) + x^{3/4}u(x) = x^{15/4} + 6x + \frac{128}{15\Gamma(1/4)}x^{9/4}, \qquad 0 \le x \le 1, \tag{82}$$

subject to

$$u(0) = 0, \qquad u'(0) = 0. \tag{83}$$

The exact solution is

$$u_{\text{exact}}(x) = x^3. \tag{84}$$

Direct symbolic substitution of Equation (84) into Equation (82) gives a zero differential-equation residual, and the two initial-condition residuals are also exactly zero.

Shifted Chebyshev Tau Method

Using N unknown coefficients, let

$$u_N(x) = \sum_{n=0}^{N-1} c_n \, T_{L,n}(x), \qquad L = 1. \tag{85}$$

The residual is

$$\begin{aligned} R_N(x) = u_N''(x) + {}^{C}D^{3/4}u_N(x) + x^{3/4}u_N(x) \\ - \left(x^{15/4} + 6x + \frac{128}{15\Gamma(1/4)} x^{9/4} \right). \end{aligned} \tag{86}$$

Since two equations are reserved for the initial conditions, the $N-2$ Tau equations are

$$\int_0^1 R_N(x) T_{L,j}(x) w_L(x) \, dx = 0, \qquad j = 0, 1, \ldots, N-3. \tag{87}$$

The remaining two equations are

$$u_N(0) = 0, \qquad u_N'(0) = 0. \tag{88}$$

Shifted Chebyshev Collocation Method

The Shifted Chebyshev Collocation Method uses the same approximation (85). The residual is forced to vanish at $N-2$ shifted Chebyshev–Gauss points:

$$R_N(x_k) = 0, \qquad k = 1, 2, \ldots, N-2, \tag{89}$$

where

$$x_k = \frac{1}{2} \left[1 + \cos\left(\frac{(2k-1)\pi}{2(N-2)} \right) \right], \qquad k = 1, 2, \ldots, N-2. \tag{90}$$

Together with the two initial conditions in Equation (88), the collocation equations form a square system of N equations for the N unknown coefficients.

Haar Wavelet Collocation Method

For the Haar formulation, the highest-order derivative is approximated by

$$u_N''(x) \simeq K_N^T H_N(x), \tag{91}$$

where $H_N(x)$ is the vector of the first N Haar basis functions and K_N denotes the unknown coefficient vector.

Using the operational matrix P_N^1, the first derivative is reconstructed as

$$u_N'(x) = K_N^T \left[P_N^1 H_N(x) - P_N^1 H_N(0) \right]. \tag{92}$$

The corrected approximate solution is

$$u_N(x) = K_N^T \left[P_N^2 H_N(x) - P_N^2 H_N(0) - x P_N^1 H_N(0)\right]. \tag{93}$$

Equations (92) and (93) ensure directly that

$$u_N(0) = 0, \qquad u_N'(0) = 0$$

independently of the unknown coefficients.

Since

$${}^C D^{3/4} u(x) = I^{5/4} u''(x)$$

under the prescribed zero initial conditions, the corrected fractional-derivative approximation is

$${}^C D^{3/4} u_N(x) = K_N^T \left[P_N^{5/4} H_N(x) - P_N^{5/4} H_N(0)\right]. \tag{94}$$

The Haar midpoint collocation points are

$$x_i = \frac{2i-1}{2N}, \qquad i = 1, 2, \ldots, N. \tag{95}$$

Substitution into the governing equation gives

$$\begin{aligned} K_N^T \Big[& H_N(x_i) + P_N^{5/4} H_N(x_i) - P_N^{5/4} H_N(0) \\ & + x_i^{3/4} \big(P_N^2 H_N(x_i) - P_N^2 H_N(0) - x_i\, P_N^1 H_N(0)\big)\Big] = g(x_i), \end{aligned} \tag{96}$$

for $i = 1, 2, \ldots, N$, where

$$g(x) = x^{15/4} + 6x + \frac{128}{15\Gamma(1/4)} x^{9/4}. \tag{97}$$

Equation (96) produces a square system of N equations for the N unknown Haar coefficients.

Computational setting and exact-polynomial reproduction

The common computational settings described in Section 6 were used. The principal results were obtained at $N = 32$.

The exact solution (84) is a polynomial of degree three. It is therefore contained in the shifted Chebyshev approximation space beginning with the smallest balanced level $N = 4$. Consequently, by Theorem 1, SCTM and SCCM reproduce the exact solution to the adopted numerical precision at every level considered.

Numerical solution comparison

Figure 13 compares the exact solution with the numerical solutions obtained by SCTM, SCCM, and HWCM at the principal balanced level $N = 32$.

The SCTM and SCCM curves are visually indistinguishable from the exact cubic profile throughout the interval. Both methods reproduce the smooth increase of the exact solution. The corrected HWCM approximation follows the same overall

behavior, although its localized piecewise structure becomes increasingly visible as x approaches 1.

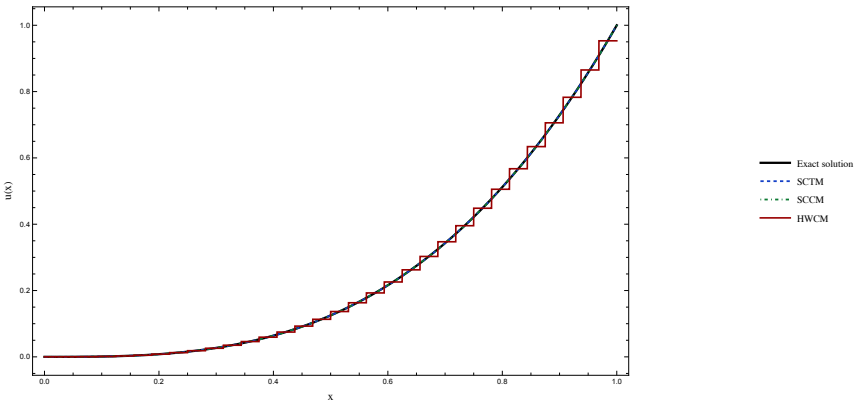

Figure 13. Comparison of the exact and numerical solutions for Example 4 at the principal balanced level $N = 32$.

The maximum absolute error and the root mean square error are listed in **Table 10**.

Table 10. Error summary for Example 4 at $N = 32$.

Method	Maximum error	RMS error
Shifted Chebyshev Tau Method	0^*	0^*
Shifted Chebyshev Collocation Method	0^*	0^*
Haar Wavelet Collocation Method	4.68870×10^{-2}	1.21436×10^{-2}

Note: *Numerically zero at the adopted working precision.

At $N = 32$, SCTM and SCCM reproduce the exact cubic solution to the adopted numerical precision. Their identical accuracy follows from the inclusion of the degree-three exact solution in the shifted Chebyshev approximation space at every balanced level.

The corrected HWCM approximation gives a maximum absolute error of 4.68870×10^{-2} and an RMS error of 1.21436×10^{-2}. The maximum error occurs near the right endpoint, where the exact solution has its largest value and steepest increase. The maximum differential-equation residual for HWCM is 2.21865×10^{-1}, while its two initial-condition residuals are numerically zero.

Balanced convergence

The balanced convergence behavior of HWCM is summarized in **Table 11**. The observed maximum-error rate is calculated from

$$r_N = \frac{\log[E_{\max}(N/2)/E_{\max}(N)]}{\log 2}. \tag{98}$$

Table 11. Balanced convergence results for HWCM in Example 4.

N	Maximum error	RMS error	Observed rate
4	3.85320×10^{-1}	1.08366×10^{-1}	–
8	1.88241×10^{-1}	4.98021×10^{-2}	1.03347
16	9.38006×10^{-2}	2.44066×10^{-2}	1.00492
32	4.68870×10^{-2}	1.21436×10^{-2}	1.00041

Figure 14 presents the corresponding balanced comparison.

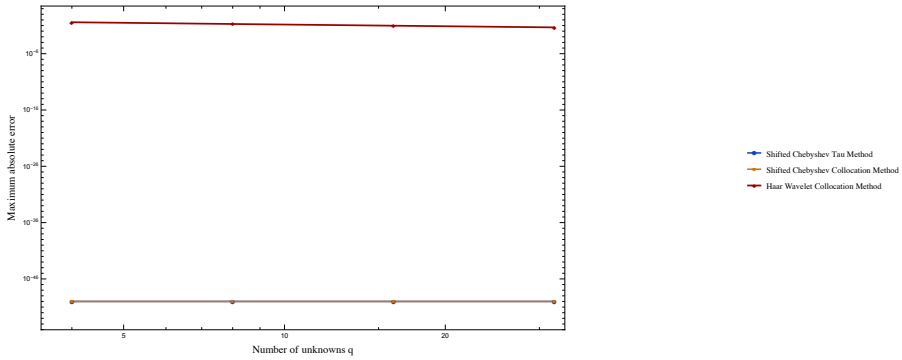

Figure 14. Balanced maximum-error comparison for Example 4 using $N = 4, 8, 16$, and 32 unknowns for every method.

The HWCM maximum error decreases by approximately one half whenever the balanced approximation size is doubled. The observed rates approach one, demonstrating approximately first-order convergence for the corrected Haar formulation.

A conventional convergence rate is not reported for SCTM and SCCM because the cubic exact solution is contained in their approximation spaces beginning with $N = 4$ and is reproduced to the adopted numerical precision at every balanced level.

Absolute-error distribution

Figure 15 shows the pointwise absolute-error distributions at $N = 32$.

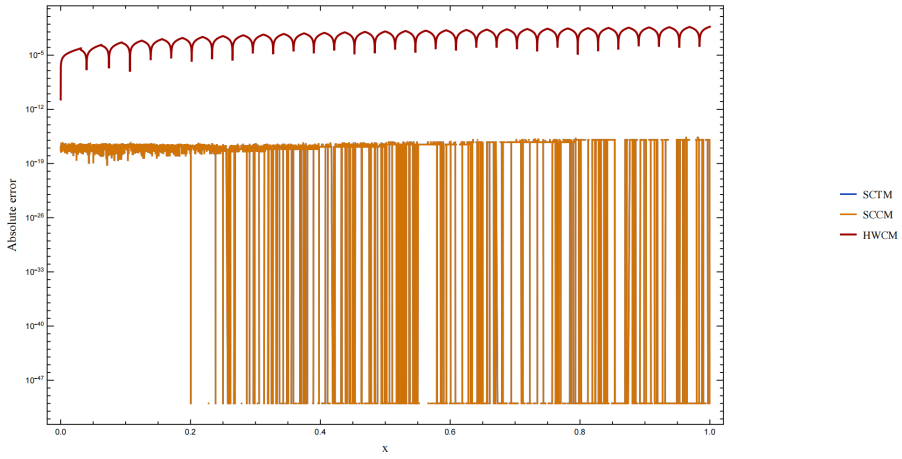

Figure 15. Pointwise absolute-error distributions for Example 4 at $N = 32$.

The SCTM and SCCM errors remain at the adopted numerical-precision level throughout the computational interval. The HWCM error displays a repeated localized pattern associated with the piecewise Haar basis. Its overall envelope increases toward the right endpoint, where the maximum pointwise error is attained.

Three-dimensional logarithmic error surfaces

The three-dimensional error results are displayed on a logarithmic scale in **Figure 16**.

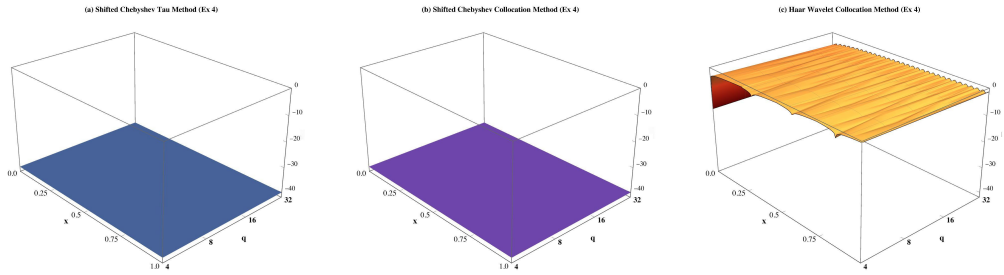

Figure 16. Three-dimensional logarithmic absolute-error surfaces for Example 4. Since the SCTM and SCCM errors are numerically zero at the adopted working precision, their panels are displayed at the fixed visualization level $\log_{10}(E) = -40$. The HWCM panel represents $\log_{10}\big(\max\{E, 10^{-16}\}\big)$. These graphical floors are introduced only for visualization and do not alter the numerical errors reported in the tables.

The SCTM and SCCM surfaces remain flat at the selected visualization floor for all balanced levels, reflecting exact polynomial reproduction to the adopted numerical precision. The HWCM surface decreases systematically as N increases. Its repeated ridges reflect the localized piecewise representation, while the declining surface height confirms the approximately first-order convergence reported in **Table 11**.

The corresponding matrix and computational diagnostics are reported in **Table 12**.

Table 12. Matrix and computational diagnostics for Example 4 at $N = 32$.

Method	$\kappa_2(A)$	Row-scaled $\kappa_2(A)$	Matrix density	Assembly time (s)	Solve time (s)	Total time (s)
Shifted Chebyshev Tau Method	8.53654×10^5	1.31085×10^5	0.999023	1.73201×10^2	5.63×10^{-4}	1.73202×10^2
Shifted Chebyshev Collocation Method	2.10017×10^6	1.00283×10^4	0.999023	3.9836×10^{-2}	6.90×10^{-4}	4.0526×10^{-2}
Haar Wavelet Collocation Method	6.31032	7.03071	0.593750	3.3402×10^{-2}	5.69×10^{-4}	3.3971×10^{-2}

The three linear-system solve times are of the same order because all systems have dimension 32×32. The main computational difference arises during matrix assembly. The weighted projection integrals make SCTM substantially more expensive in the present implementation. SCCM and HWCM have comparable total times, with HWCM giving the shortest total time in this example.

Overall, Example 4 confirms the substantially higher accuracy of the two shifted Chebyshev formulations for this smooth cubic benchmark. The corrected HWCM approximation preserves the global cubic profile, satisfies both initial conditions exactly, and converges regularly with an observed rate approaching one. Although its approximation error is larger, the HWCM coefficient matrix is considerably better conditioned and less dense.

7.5. Example 5

The fifth test problem contains the fractional-power term $x^{5/2}$ in the forcing function. Thus, although the exact solution remains a smooth cubic polynomial, the right-hand side is not restricted to integer powers of x. This example therefore examines how the three numerical formulations handle a combination of integer-order and fractional-order operators with a nonpolynomial forcing term.

Consider

$$u''(x) - 2u'(x) + {}^{C}D^{1/2}u(x) + xu(x) = x^4 - 6x^2 + 6x + \tfrac{16}{5\sqrt{\pi}}x^{5/2}, \qquad 0 \le x \le 1, \tag{99}$$

subject to

$$u(0) = 0, \qquad u'(0) = 0. \tag{100}$$

The exact solution is

$$u_{\text{exact}}(x) = x^3. \tag{101}$$

Indeed,

$$u'_{\text{exact}}(x) = 3x^2, \qquad u''_{\text{exact}}(x) = 6x,$$

and

$${}^{C}D^{1/2}x^3 = \frac{\Gamma(4)}{\Gamma(7/2)}x^{5/2} = \frac{16}{5\sqrt{\pi}}x^{5/2}.$$

Consequently, direct substitution of Equation (101) into Equation (99) gives an identically zero differential-equation residual, and both initial conditions are satisfied exactly.

Shifted Chebyshev Tau Method

Using N unknown coefficients, the approximate solution is written as

$$u_N(x) = \sum_{n=0}^{N-1} c_n\, T_{L,n}(x), \qquad L = 1. \tag{102}$$

The corresponding residual is

$$\begin{aligned} R_N(x) = {} & u''_N(x) - 2u'_N(x) + {}^{C}D^{1/2}u_N(x) + xu_N(x) \\ & - \left(x^4 - 6x^2 + 6x + \frac{16}{5\sqrt{\pi}}x^{5/2}\right). \end{aligned} \tag{103}$$

Since two equations are reserved for the initial conditions, the $N-2$ Tau equations are

$$\int_0^1 R_N(x) T_{L,j}(x) w_L(x)\, dx = 0, \qquad j = 0, 1, \ldots, N-3. \tag{104}$$

The remaining equations are

$$u_N(0) = 0, \qquad u'_N(0) = 0. \tag{105}$$

Shifted Chebyshev Collocation Method

The Shifted Chebyshev Collocation Method uses the same approximation (102). The residual is forced to vanish at $N-2$ shifted Chebyshev–Gauss points:

$$R_N(x_k) = 0, \qquad k = 1, 2, \ldots, N-2, \tag{106}$$

where

$$x_k = \frac{1}{2}\left[1 + \cos\left(\frac{(2k-1)\pi}{2(N-2)}\right)\right], \qquad k = 1, 2, \ldots, N-2. \tag{107}$$

Together with the two conditions in Equation (105), these equations produce a square system of N equations for the N unknown coefficients.

Haar Wavelet Collocation Method

For the Haar formulation, the highest-order derivative is approximated by

$$u_N''(x) \simeq K_N^T H_N(x), \tag{108}$$

where $H_N(x)$ is the vector of the first N Haar basis functions and K_N is the vector of unknown coefficients.

Using the Haar operational matrix P_N^1, the first derivative is reconstructed as

$$u_N'(x) = K_N^T \left[P_N^1 H_N(x) - P_N^1 H_N(0)\right]. \tag{109}$$

The endpoint-corrected approximation of the Caputo derivative is

$${}^C D^{1/2} u_N(x) = K_N^T \left[P_N^{3/2} H_N(x) - P_N^{3/2} H_N(0)\right]. \tag{110}$$

The approximate solution is reconstructed as

$$u_N(x) = K_N^T \left[P_N^2 H_N(x) - P_N^2 H_N(0) - x P_N^1 H_N(0)\right]. \tag{111}$$

Equations (109) and (111) ensure directly that

$$u_N(0) = 0, \qquad u_N'(0) = 0$$

independently of the unknown coefficient values.

At the Haar midpoint collocation points

$$x_i = \frac{2i-1}{2N}, \qquad i = 1, 2, \ldots, N, \tag{112}$$

substitution into the governing equation gives

$$\begin{aligned} K_N^T \Big[& H_N(x_i) - 2\left(P_N^1 H_N(x_i) - P_N^1 H_N(0)\right) \\ & + P_N^{3/2} H_N(x_i) - P_N^{3/2} H_N(0) \\ & + x_i \left(P_N^2 H_N(x_i) - P_N^2 H_N(0) - x_i\, P_N^1 H_N(0)\right) \Big] = g(x_i), \end{aligned} \tag{113}$$

for $i = 1, 2, \ldots, N$, where

$$g(x) = x^4 - 6x^2 + 6x + \frac{16}{5\sqrt{\pi}} x^{5/2}. \tag{114}$$

Equation (113) produces a square system of N equations for the N unknown Haar coefficients.

Computational setting and exact-polynomial reproduction

The common computational settings described in Section 6 were used. The principal numerical results were obtained at $N = 32$.

The exact solution (101) is a polynomial of degree three. It therefore belongs to the shifted Chebyshev approximation space beginning with the smallest balanced level

$N = 4$. Consequently, by Theorem 1, SCTM and SCCM reproduce the exact solution to the adopted numerical precision at every balanced level considered.

Numerical solution comparison

Figure 17 compares the exact solution with the numerical solutions obtained by SCTM, SCCM, and HWCM at the principal balanced level $N = 32$.

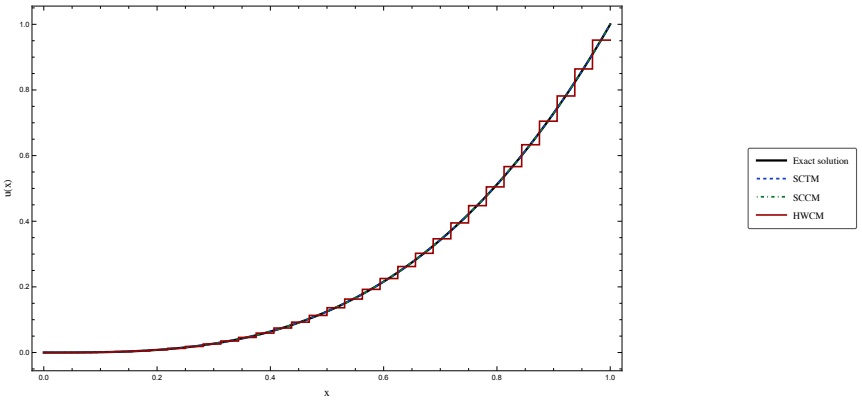

Figure 17. Comparison of the exact and numerical solutions for Example 5 at the principal balanced level $N = 32$.

The SCTM and SCCM curves are visually indistinguishable from the exact cubic profile over the full computational interval. The corrected HWCM approximation follows the same increasing shape, although its localized piecewise structure becomes more visible near the upper end of the interval.

The maximum absolute error and root mean square error are listed in **Table 13**.

Table 13. Error summary for Example 5 at $N = 32$.

Method	Maximum error	RMS error
Shifted Chebyshev Tau Method	0^*	0^*
Shifted Chebyshev Collocation Method	0^*	0^*
Haar Wavelet Collocation Method	4.81645×10^{-2}	1.21875×10^{-2}

Note: *Numerically zero at the adopted working precision.

At $N = 32$, SCTM and SCCM reproduce the exact cubic solution to the adopted numerical precision. The corrected HWCM approximation gives a maximum absolute error of 4.81645×10^{-2} and an RMS error of 1.21875×10^{-2}. The largest pointwise error occurs near $x = 1$. Its maximum differential-equation residual is 9.23407×10^{-2}, while both initial-condition residuals are numerically zero.

Balanced convergence

The balanced convergence behavior of HWCM is summarized in **Table 14**. The observed rates were computed using Equation (32).

Table 14. Balanced convergence results for HWCM in Example 5.

N	Maximum error	RMS error	Observed rate
4	4.22974×10^{-1}	1.16272×10^{-1}	–
8	2.03360×10^{-1}	5.15320×10^{-2}	1.05653

Table 14. *Cont.*

N	Maximum error	RMS error	Observed rate
16	9.84344×10^{-2}	2.46967×10^{-2}	1.04680
32	4.81645×10^{-2}	1.21875×10^{-2}	1.03119

Figure 18 presents the corresponding balanced maximum-error comparison.

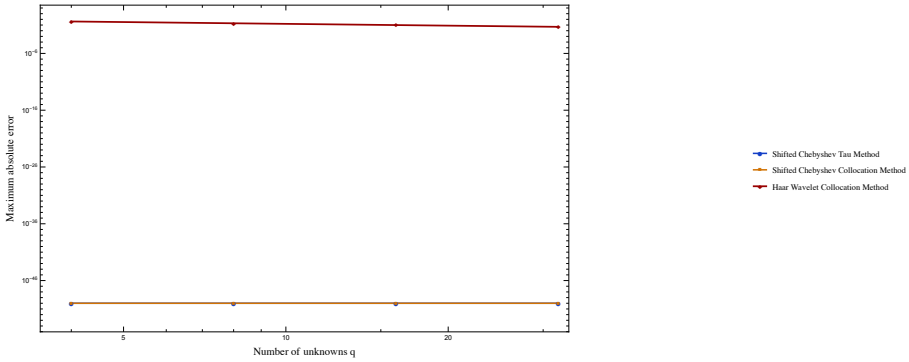

Figure 18. Balanced maximum-error comparison for Example 5 using $N = 4, 8, 16$, and 32 unknowns for every method.

The HWCM maximum error decreases by approximately one half whenever the balanced approximation size is doubled. The observed rates remain slightly above one and approach unity as N increases, indicating approximately first-order convergence.

A conventional convergence rate is not reported for SCTM and SCCM because the cubic exact solution is contained in their approximation spaces at every balanced level and is reproduced to the adopted numerical precision.

Absolute-error distribution

Figure 19 displays the pointwise absolute-error distributions at $N = 32$.

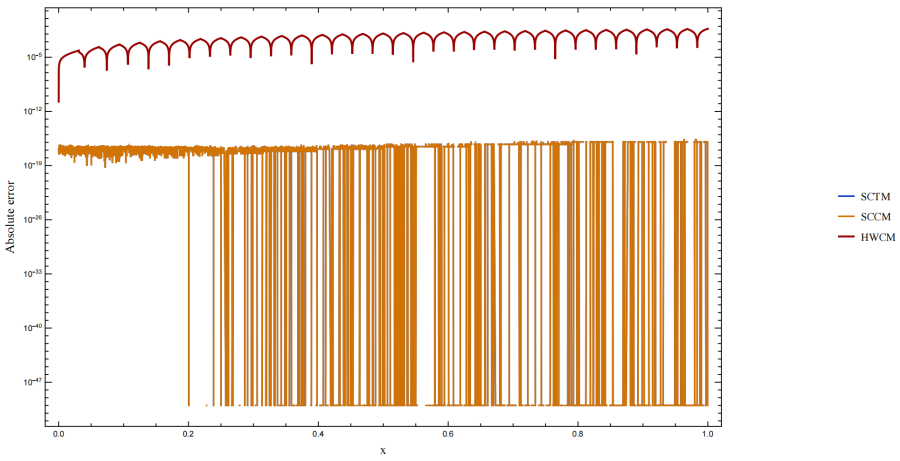

Figure 19. Pointwise absolute-error distributions for Example 5 at $N = 32$.

The SCTM and SCCM errors remain at the adopted numerical-precision level throughout the computational interval. The HWCM error exhibits a repeated localized pattern generated by the piecewise Haar basis. Its overall envelope increases toward the right endpoint.

Three-dimensional logarithmic error surfaces

The variation of the numerical errors with both the spatial coordinate and the balanced approximation size is displayed in **Figure 20**.

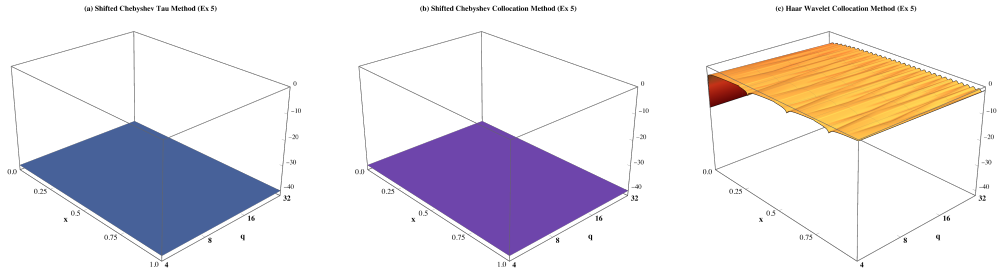

Figure 20. Three-dimensional logarithmic absolute-error surfaces for Example 5. Since the SCTM and SCCM errors are below the adopted graphical precision threshold, their panels are displayed at the fixed level $\log_{10}(E) = -40$. The HWCM panel displays $\log_{10}\big(\max\{E, 10^{-16}\}\big)$ using the computed errors. These graphical floors are introduced solely for visualization and do not modify the reported numerical results.

The SCTM and SCCM surfaces remain flat at the selected visualization floor for every balanced level, reflecting exact polynomial reproduction to the adopted numerical precision. The HWCM surface decreases systematically as N increases, while its repeated ridges reflect the localized piecewise basis.

The matrix and computational diagnostics are reported in **Table 15**.

Table 15. Matrix and computational diagnostics for Example 5 at $N = 32$.

Method	$\kappa_2(A)$	Row-scaled $\kappa_2(A)$	Matrix density	Assembly time (s)	Solve time (s)	Total time (s)
Shifted Chebyshev Tau Method	1.28946×10^6	2.94704×10^5	0.971680	3.58218×10^1	5.22×10^{-4}	3.58223×10^1
Shifted Chebyshev Collocation Method	3.14799×10^6	2.89007×10^4	0.999023	2.5265×10^{-2}	4.66×10^{-4}	2.5731×10^{-2}
Haar Wavelet Collocation Method	3.69247	3.98997	0.593750	3.3551×10^{-2}	5.31×10^{-4}	3.4082×10^{-2}

The three solution times are of the same order because all coefficient systems have dimension 32×32. The principal computational difference occurs during matrix assembly. SCTM is substantially more expensive because of the weighted projection integrals. SCCM has the smallest total time, whereas HWCM requires a slightly larger total time but produces a substantially better-conditioned and less dense coefficient matrix.

Overall, Example 5 confirms the higher accuracy of the two shifted Chebyshev formulations for this smooth cubic solution. HWCM preserves the global solution profile, satisfies both initial conditions exactly, and converges regularly with an observed rate approaching one, while offering clear advantages in matrix conditioning and sparsity.

7.6. Example 6: Low-regularity fractional-power benchmark

The sixth example investigates the influence of reduced endpoint regularity on the performance of the three numerical formulations. Unlike the preceding polynomial benchmarks, the exact solution cannot be represented exactly by any finite shifted Chebyshev expansion. Consequently, the problem provides a genuine convergence test for SCTM, SCCM, and HWCM.

Consider the fractional initial-value problem

$$u''(x) + {}^{C}D_{0+}^{3/4}u(x) + u(x) = \frac{15}{4}x^{1/2} + \frac{\Gamma\left(\frac{7}{2}\right)}{\Gamma\left(\frac{11}{4}\right)}x^{7/4} + x^{5/2}, \qquad 0 < x \leq 1, \tag{115}$$

subject to

$$u(0) = 0, \qquad u'(0) = 0. \tag{116}$$

The exact solution is

$$u_{\text{exact}}(x) = x^{5/2}. \tag{117}$$

For this power function,

$${}^{C}D_{0+}^{3/4}x^{5/2} = \frac{\Gamma\left(\frac{7}{2}\right)}{\Gamma\left(\frac{11}{4}\right)}x^{7/4}. \tag{118}$$

Moreover,

$$u'_{\text{exact}}(x) = \frac{5}{2}x^{3/2}, \qquad u''_{\text{exact}}(x) = \frac{15}{4}x^{1/2}. \tag{119}$$

Consequently, direct substitution of Equation (117) into Equation (115) gives an identically zero differential-equation residual, and both prescribed initial conditions are satisfied exactly.

The reduced endpoint regularity follows from

$$u^{(3)}_{\text{exact}}(x) = \frac{15}{8}x^{-1/2}, \tag{120}$$

so that

$$\lim_{x\to 0^+} u^{(3)}_{\text{exact}}(x) = +\infty. \tag{121}$$

Thus,

$$u_{\text{exact}} \in C^2[0,1], \qquad u_{\text{exact}} \notin C^3[0,1]. \tag{122}$$

This loss of higher-order endpoint regularity distinguishes Example 6 from the smooth polynomial benchmarks considered previously.

Shifted Chebyshev Tau Method

Using N unknown coefficients, the approximation is written as

$$u_N(x) = \sum_{n=0}^{N-1} a_n\, T_{L,n}(x), \qquad L = 1. \tag{123}$$

The corresponding residual is

$$\begin{aligned} R_N(x) = {} & u''_N(x) + {}^{C}D_{0+}^{3/4}u_N(x) + u_N(x) \\ & - \left[\frac{15}{4}x^{1/2} + \frac{\Gamma\left(\frac{7}{2}\right)}{\Gamma\left(\frac{11}{4}\right)}x^{7/4} + x^{5/2}\right]. \end{aligned} \tag{124}$$

Since two equations are reserved for the initial conditions, the $N-2$ weighted

Tau equations are

$$\int_0^1 R_N(x)T_{L,j}(x)w_L(x)\,dx = 0, \qquad j = 0, 1, \ldots, N-3. \tag{125}$$

The remaining equations are

$$u_N(0) = 0, \qquad u'_N(0) = 0. \tag{126}$$

The Caputo derivatives of the shifted Chebyshev basis functions are evaluated by expanding each polynomial in monomial form and applying the fractional power rule term by term.

Shifted Chebyshev Collocation Method

The Shifted Chebyshev Collocation Method uses the same approximation (123). The residual is imposed at $N-2$ shifted Chebyshev–Gauss points:

$$R_N(x_k) = 0, \qquad k = 1, 2, \ldots, N-2, \tag{127}$$

where

$$x_k = \frac{1}{2}\left[1 + \cos\left(\frac{(2k-1)\pi}{2(N-2)}\right)\right], \qquad k = 1, 2, \ldots, N-2. \tag{128}$$

Together with Equation (126), these equations produce a square system of N equations for the N unknown coefficients.

Haar Wavelet Collocation Method

For the Haar formulation, the second derivative is approximated by

$$u''_N(x) \simeq K_N^T H_N(x), \tag{129}$$

where $H_N(x)$ denotes the vector of the first N Haar basis functions and K_N is the unknown coefficient vector.

The first derivative is reconstructed as

$$u'_N(x) = K_N^T \left[P_N^1 H_N(x) - P_N^1 H_N(0)\right]. \tag{130}$$

The corrected approximate solution is

$$u_N(x) = K_N^T \left[P_N^2 H_N(x) - P_N^2 H_N(0) - xP_N^1 H_N(0)\right]. \tag{131}$$

These representations enforce

$$u_N(0) = 0, \qquad u'_N(0) = 0$$

independently of the unknown coefficients.

Because $u'_N(0) = 0$, the Caputo derivative may be represented as

$${}^C D_{0+}^{3/4} u_N(x) = I_{0+}^{5/4} u''_N(x). \tag{132}$$

Its endpoint-corrected Haar approximation is

$$ {}^{C}D_{0+}^{3/4}u_N(x) = K_N^T \left[P_N^{5/4} H_N(x) - P_N^{5/4} H_N(0) \right]. \tag{133} $$

At the Haar midpoint collocation points

$$ x_i = \frac{2i-1}{2N}, \qquad i = 1, 2, \ldots, N, \tag{134} $$

the coefficient vector K_N is determined from

$$ \begin{aligned} K_N^T \Big[& H_N(x_i) + P_N^{5/4} H_N(x_i) - P_N^{5/4} H_N(0) \\ & + P_N^2 H_N(x_i) - P_N^2 H_N(0) - x_i \, P_N^1 H_N(0) \Big] = f(x_i), \end{aligned} \tag{135} $$

for $i = 1, 2, \ldots, N$, where

$$ f(x) = \frac{15}{4} x^{1/2} + \frac{\Gamma\left(\frac{7}{2}\right)}{\Gamma\left(\frac{11}{4}\right)} x^{7/4} + x^{5/2}. \tag{136} $$

Equation (135) produces a square system of N equations for the N unknown Haar coefficients.

Computational setting

The common computational settings described in Section 6 were used. The principal results were obtained at $N = 32$.

Unlike the preceding polynomial benchmarks, the exact solution $x^{5/2}$ does not belong to any finite shifted Chebyshev polynomial space. Consequently, all three methods produce nonzero approximation errors and meaningful observed convergence rates.

Numerical solution comparison

Figure 21 compares the exact solution with the three numerical approximations at $N = 32$.

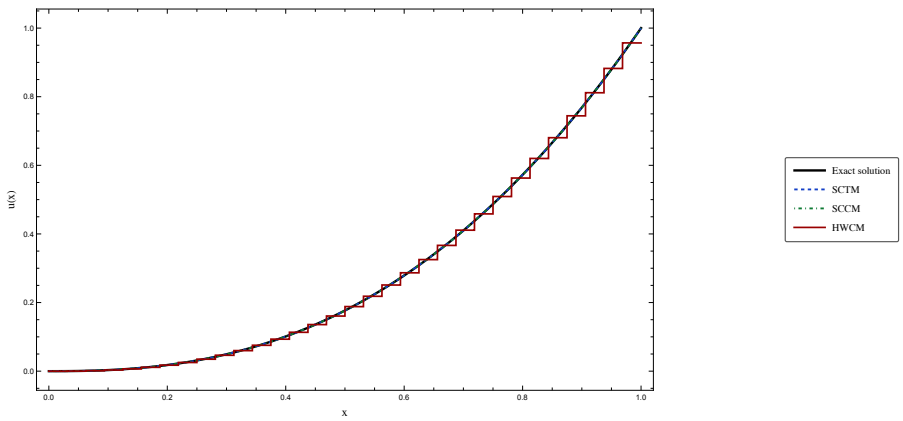

Figure 21. Comparison of the exact and numerical solutions for the low-regularity benchmark in Example 6 at $N = 32$.

The SCTM and SCCM approximations are visually indistinguishable from the

exact fractional-power profile. The corrected HWCM approximation preserves the same global increasing behavior, although its localized piecewise structure becomes more visible toward the right endpoint.

The principal accuracy and residual measures are reported in **Table 16**.

Table 16. Accuracy and residual measures for Example 6 at $N = 32$.

Method	Maximum error	RMS error	x at maximum error	Maximum PDE residual	Maximum IC residual
Shifted Chebyshev Tau Method	4.39523×10^{-6}	3.11477×10^{-6}	0.990500	4.05150×10^{-2}	0^*
Shifted Chebyshev Collocation Method	4.31475×10^{-6}	3.05058×10^{-6}	1.00000	6.25159×10^{-2}	0^*
Haar Wavelet Collocation Method	4.33493×10^{-2}	1.17675×10^{-2}	1.00000	4.70322×10^{-1}	0^*

Note: * Numerically zero at the adopted working precision.

At $N = 32$, SCTM and SCCM attain maximum errors of order 10^{-6}. SCCM gives marginally smaller maximum and RMS errors than SCTM, although the two methods exhibit comparable high-order accuracy. HWCM gives a maximum error of 4.33493×10^{-2} and an RMS error of 1.17675×10^{-2}.

All three methods satisfy the prescribed initial conditions to the adopted precision. The differential-equation residuals are larger than the solution errors because the residual contains derivative terms, which are more sensitive to the reduced endpoint regularity.

Matrix and computational diagnostics

Table 17 reports the matrix properties and computational times at $N = 32$.

Table 17. Matrix and computational diagnostics for Example 6 at $N = 32$.

Method	$\kappa_2(A)$	Row-scaled $\kappa_2(A)$	Rank	Matrix density	Assembly time (s)	Solve time (s)	Total time (s)
Shifted Chebyshev Tau Method	7.79354×10^5	1.27763×10^5	32	0.970703	1.52007×10^2	5.54×10^{-4}	1.52008×10^2
Shifted Chebyshev Collocation Method	1.91806×10^6	9.45341×10^3	32	0.999023	3.1533×10^{-2}	4.87×10^{-4}	3.2020×10^{-2}
Haar Wavelet Collocation Method	6.45272	7.16191	32	0.593750	3.2324×10^{-2}	5.42×10^{-4}	3.2866×10^{-2}

All three coefficient matrices have full numerical rank. The solution times are of the same order because each system has dimension 32×32. The principal timing difference occurs during matrix assembly. SCTM requires approximately 152.008 seconds, whereas SCCM and HWCM require approximately 3.2020×10^{-2} and 3.2866×10^{-2} s, respectively.

The reported CPU times were obtained within the same Mathematica session and are intended as relative implementation-cost indicators rather than machine-independent complexity measures.

Balanced convergence

The observed rates were computed using Equation (32). The balanced maximum-error results are summarized in **Table 18**.

Table 18. Balanced maximum-error convergence results for Example 6.

N	SCTM error	SCTM rate	SCCM error	SCCM rate	HWCM error	HWCM rate
4	5.46238×10^{-2}	–	1.67015×10^{-2}	–	4.00311×10^{-1}	–
8	7.90468×10^{-4}	6.11068	5.39144×10^{-4}	4.95316	1.86810×10^{-1}	1.09955
16	4.65981×10^{-5}	4.08436	4.25032×10^{-5}	3.66503	8.95181×10^{-2}	1.06132
32	4.39523×10^{-6}	3.40626	4.31475×10^{-6}	3.30022	4.33493×10^{-2}	1.04617

For completeness, the corresponding RMS errors are in the following **Table 19**.

Table 19. RMS errors for Example 6.

Methods	$N = 4$	$N = 8$	$N = 16$	$N = 32$
SCTM	2.55464×10^{-2}	5.15208×10^{-4}	3.29068×10^{-5}	3.11477×10^{-6}
SCCM	7.45309×10^{-3}	3.82876×10^{-4}	3.00143×10^{-5}	3.05058×10^{-6}
HWCM	1.24900×10^{-1}	5.28840×10^{-2}	2.44723×10^{-2}	1.17675×10^{-2}

Figure 22 presents the balanced maximum-error comparison.

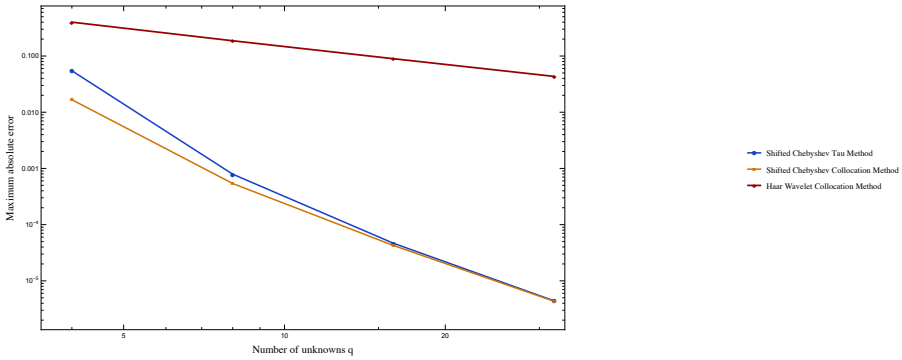

Figure 22. Balanced maximum-error comparison for Example 6 using $N = 4, 8, 16$, and 32 unknowns for every method.

The final observed rates are 3.40626 for SCTM, 3.30022 for SCCM, and 1.04617 for HWCM. Thus, over the tested balanced levels, the two shifted Chebyshev methods exhibit high-order algebraic convergence, whereas HWCM exhibits stable first-order-type convergence.

These observed results should not be interpreted as a complete asymptotic convergence proof. They nevertheless demonstrate that the Chebyshev errors decrease substantially more rapidly than the Haar errors over the approximation sizes considered.

Absolute-error distribution

Figure 23 displays the pointwise absolute-error distributions at $N = 32$.

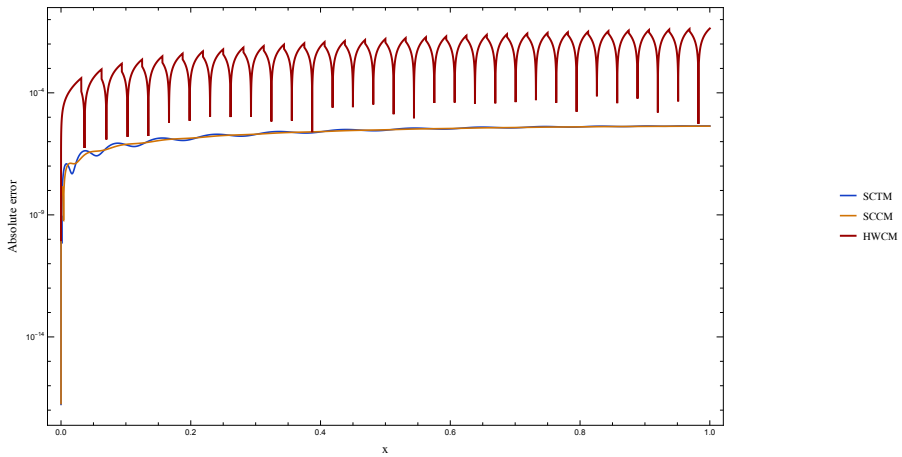

Figure 23. Pointwise absolute-error distributions for Example 6 at $N = 32$.

The SCTM and SCCM error curves have comparable magnitudes and remain of order 10^{-6} over most of the computational interval. Their largest errors occur close to

the right endpoint. The HWCM error is larger and exhibits repeated localized minima and peaks associated with the dyadic Haar partitions.

Three-dimensional logarithmic error surfaces

Figure 24 displays the computed errors for all three methods over the balanced approximation sizes.

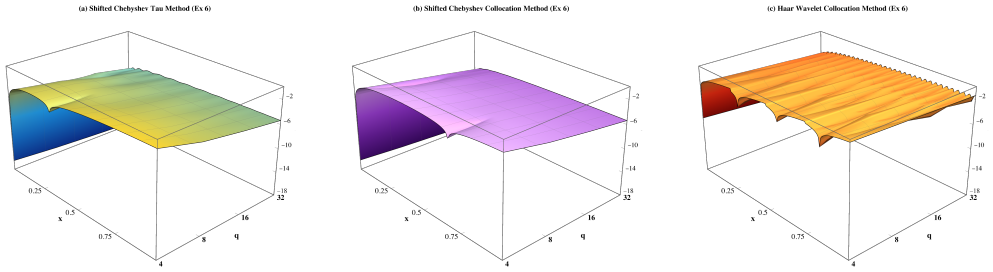

Figure 24. Three-dimensional logarithmic absolute-error surfaces for Example 6. The vertical coordinate represents $\log_{10}\big(\max\{|u_{\text{exact}}(x) - u_N(x)|, 10^{-18}\}\big)$. The positive floor is introduced only to display zero or near-zero values on a finite logarithmic scale.

Unlike the preceding polynomial benchmarks, all three panels represent genuine nonzero approximation errors. The SCTM and SCCM surfaces decay rapidly as N increases, whereas the HWCM surface decreases more gradually. The repeated Haar ridges reflect the localized dyadic partition rather than a failure of convergence.

Overall, Example 6 distinguishes approximation accuracy from algebraic efficiency. SCTM and SCCM retain high-order accuracy despite the reduced endpoint regularity, with SCCM achieving a marginally smaller error and a substantially lower assembly cost. HWCM is less accurate at the same number of unknowns but produces a considerably better-conditioned and less dense system together with regular first-order-type convergence.

Remark 1. *Example 6 shows that the high accuracy of SCTM and SCCM in the preceding examples is not solely a consequence of exact polynomial reproduction. For the nonpolynomial solution $x^{5/2}$, both methods retain high-order convergence and achieve maximum errors of order 10^{-6} using 32 unknown coefficients. HWCM gives a larger error but maintains approximately first-order convergence, markedly better matrix conditioning, and greater sparsity. The example therefore demonstrates a clear trade-off between approximation accuracy and algebraic structure.*

8. Overall computational and matrix-structure comparison

This section consolidates the matrix-structure and computational results obtained for the six benchmark problems. The purpose is to identify the principal differences among the three methods without repeating the detailed numerical discussions presented in Examples 1–6.

For a coefficient matrix $A \in \mathbb{R}^{N\times N}$, the matrix density used in this study is defined by

$$\rho(A) = \frac{\text{nnz}(A)}{N^2}, \tag{137}$$

where $\mathrm{nnz}(A)$ denotes the number of entries that remain nonzero after applying the adopted numerical tolerance. The corresponding sparsity ratio is

$$s(A) = 1 - \rho(A). \tag{138}$$

All matrix structures and computational quantities reported in this section correspond to the principal balanced level $N = 32$. The condition numbers are spectral two-norm condition numbers, and the reported CPU times were obtained within the same Mathematica session. They are therefore interpreted as relative implementation-cost indicators rather than machine-independent complexity measures.

8.1. Coefficient-matrix structures

Figures 25–30 display the coefficient-matrix structures produced by SCTM, SCCM, and HWCM in the six benchmark problems.

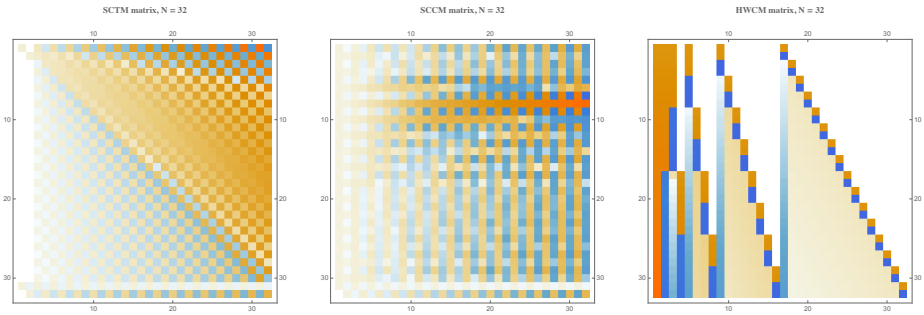

Figure 25. Coefficient-matrix structures for SCTM, SCCM, and HWCM in Example 1 at $N = 32$.

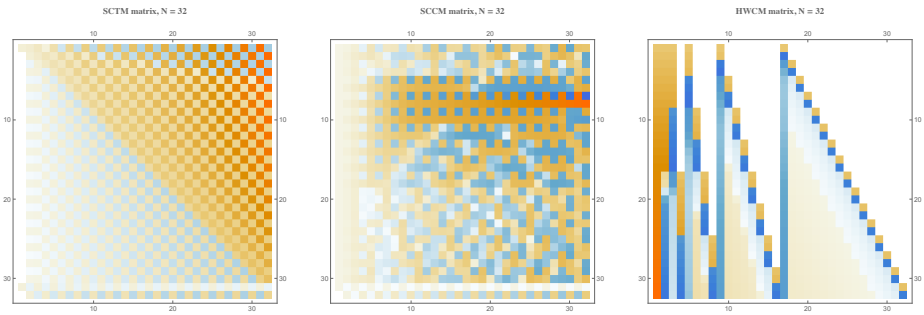

Figure 26. Coefficient-matrix structures for SCTM, SCCM, and HWCM in Example 2 at $N = 32$.

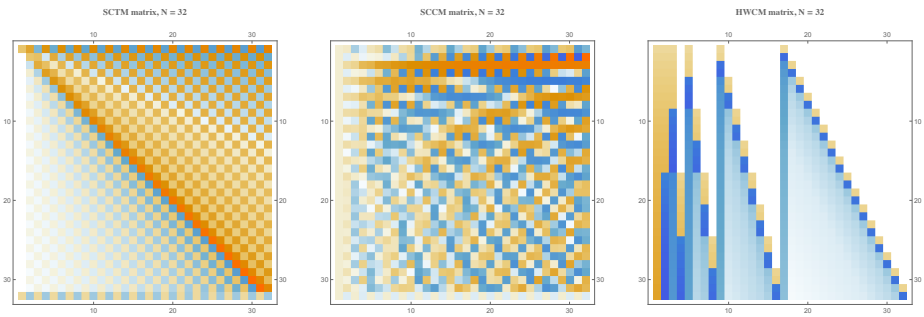

Figure 27. Coefficient-matrix structures for SCTM, SCCM, and HWCM in Example 3 at $N = 32$.

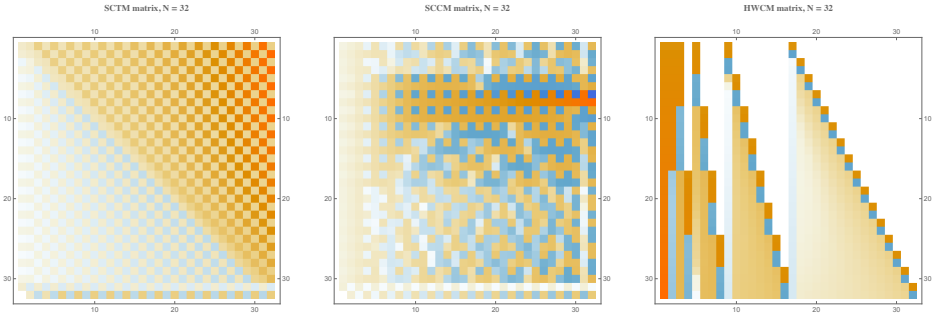

Figure 28. Coefficient-matrix structures for SCTM, SCCM, and HWCM in Example 4 at $N = 32$.

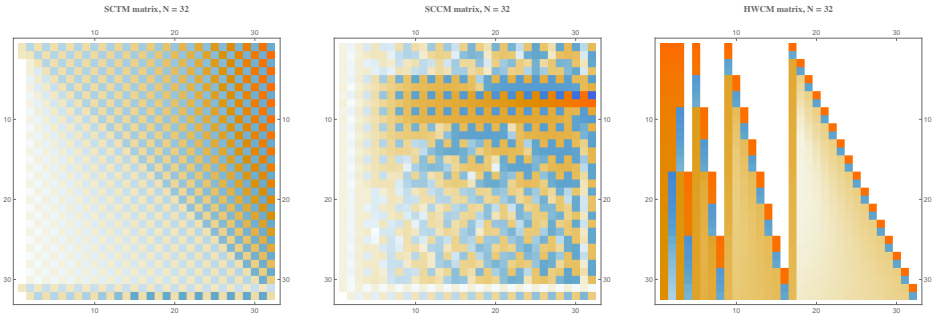

Figure 29. Coefficient-matrix structures for SCTM, SCCM, and HWCM in Example 5 at $N = 32$.

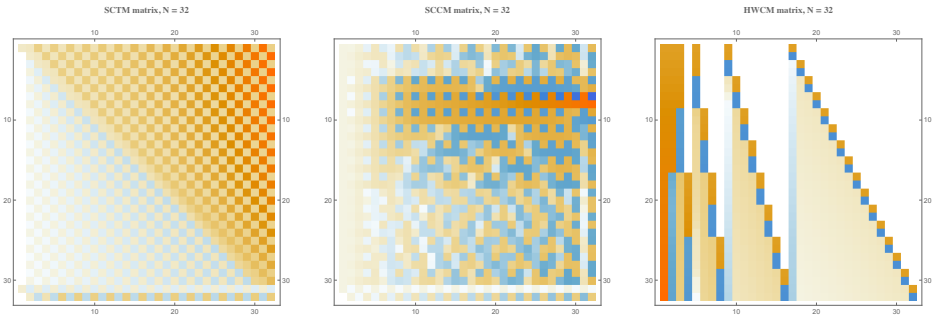

Figure 30. Coefficient-matrix structures for SCTM, SCCM, and HWCM in the low-regularity benchmark of Example 6 at $N = 32$.

The matrix plots reveal a consistent structural distinction among the three formulations. The SCTM and SCCM coefficient matrices are predominantly dense because the shifted Chebyshev basis functions have global support. At $N = 32$, their observed densities range from 0.942383 to 1.000000.

In contrast, the HWCM matrices have an observed density of 0.593750 in all six experiments, corresponding to a sparsity ratio of

$$1 - 0.593750 = 0.406250,$$

or 40.625%. Their visible block and band structures reflect the localized support and dyadic organization of the Haar basis functions.

The conditioning results exhibit the same general pattern. The unscaled SCTM condition numbers range from 3.54783×10^1 to 1.28946×10^6, while the SCCM

condition numbers range from 8.40856×10^1 to 3.14799×10^6. By comparison, the HWCM condition numbers remain between 3.69247 and 1.03747×10^1. Thus, the Haar systems are consistently better conditioned in the reported experiments, even though their approximation errors are generally larger at the same value of N.

8.2. Unified numerical and computational summary

The principal numerical and computational results at $N = 32$ are collected in **Table 20**. The table reports the maximum absolute error, root mean square error, final observed convergence rate, spectral two-norm condition number, coefficient matrix density, and total computational time.

Table 20. Overall numerical and computational comparison at the principal balanced level $N = 32$.

Example	Method	Maximum error	RMS error	Observed rate	$\kappa_2(A)$	Matrix density	Total time (s)
Example 1	SCTM	0^*	0^*	–	3.46237×10^4	0.942383	4.80631
Example 1	SCCM	0^*	0^*	–	7.81378×10^4	0.999023	1.6543×10^{-2}
Example 1	HWCM	5.86881×10^{-2}	2.07534×10^{-2}	1.00381	5.03740	0.593750	3.3016×10^{-2}
Example 2	SCTM	0^*	0^*	–	8.46790×10^5	0.970703	3.98986×10^1
Example 2	SCCM	0^*	0^*	–	2.09115×10^6	0.999023	2.5618×10^{-2}
Example 2	HWCM	3.71425×10^{-2}	1.11536×10^{-2}	0.607724	1.03747×10^1	0.593750	4.5643×10^{-2}
Example 3	SCTM	0^*	0^*	–	3.54783×10^1	0.970703	2.15304×10^1
Example 3	SCCM	0^*	0^*	–	8.40856×10^1	1.000000	2.1568×10^{-2}
Example 3	HWCM	3.75539×10^{-2}	7.74609×10^{-3}	0.943922	6.32541	0.593750	2.2801×10^{-2}
Example 4	SCTM	0^*	0^*	–	8.53654×10^5	0.999023	1.73202×10^2
Example 4	SCCM	0^*	0^*	–	2.10017×10^6	0.999023	4.0526×10^{-2}
Example 4	HWCM	4.68870×10^{-2}	1.21436×10^{-2}	1.00041	6.31032	0.593750	3.3971×10^{-2}
Example 5	SCTM	0^*	0^*	–	1.28946×10^6	0.971680	3.58223×10^1
Example 5	SCCM	0^*	0^*	–	3.14799×10^6	0.999023	2.5731×10^{-2}
Example 5	HWCM	4.81645×10^{-2}	1.21875×10^{-2}	1.03119	3.69247	0.593750	3.4082×10^{-2}
Example 6	SCTM	4.39523×10^{-6}	3.11477×10^{-6}	3.40626	7.79354×10^5	0.970703	1.52008×10^2
Example 6	SCCM	4.31475×10^{-6}	3.05058×10^{-6}	3.30022	1.91806×10^6	0.999023	3.2020×10^{-2}
Example 6	HWCM	4.33493×10^{-2}	1.17675×10^{-2}	1.04617	6.45272	0.593750	3.2866×10^{-2}

Note: *Numerically zero at the adopted working precision. The symbol "–" indicates that a conventional observed rate is not reported because the corresponding polynomial solution is recovered to the adopted numerical precision. CPU times are implementation-dependent and are used only as relative indicators obtained within the same Mathematica session.

8.3. Overall interpretation

Table 20 reveals two distinct numerical regimes. In Examples 1–5, the exact solutions are polynomials. At the principal balanced level $N = 32$, each exact solution belongs to the shifted Chebyshev approximation space. Consequently, SCTM and SCCM recover these solutions to the adopted working precision. This behavior reflects finite-dimensional polynomial reproduction and should not be interpreted as exact performance for arbitrary fractional differential equations.

Example 6 provides the essential nonpolynomial low-regularity test. For

$$u_{\text{exact}}(x) = x^{5/2},$$

neither shifted Chebyshev method can achieve exact recovery in a finite polynomial space. Nevertheless, SCTM and SCCM attain maximum errors of 4.39523×10^{-6} and 4.31475×10^{-6}, respectively, at $N = 32$. Their final observed rates are 3.40626

and 3.30022, indicating high-order algebraic convergence over the balanced levels considered.

HWCM produces larger errors at the same number of unknowns. Its final observed rates are close to one in Examples 1, 3–6, indicating regular first-order-type convergence. Example 2 has a lower final rate of 0.607724, showing that the observed Haar convergence can depend on the combination of derivative orders and operators in the governing equation.

The algebraic diagnostics lead to a different comparison. The HWCM matrices are consistently less dense and substantially better conditioned than the shifted Chebyshev matrices. At $N = 32$, HWCM condition numbers remain of order 10^0 to 10^1, whereas the SCTM and SCCM condition numbers reach order 10^6 in several examples.

The linear-system solution times are similar because all three methods use coefficient systems of the same dimension. The dominant difference occurs during matrix assembly. The weighted projection integrals make SCTM the most expensive formulation in every example. SCCM avoids these integrations and gives the smallest total time in five of the six examples. HWCM has a comparable total cost while retaining its advantages in conditioning and sparsity.

Overall, the numerical evidence demonstrates an accuracy–structure trade-off. SCTM and SCCM are preferable for the present benchmarks when high approximation accuracy is the principal objective. SCCM is particularly attractive because it retains accuracy comparable to SCTM with substantially lower assembly cost. HWCM is less accurate at the same balanced size but produces more favorable matrix structures and stable algebraic convergence.

These conclusions are restricted to the selected polynomial and low-regularity fractional-power benchmarks. They should not be interpreted as a universal ranking for arbitrary fractional differential equations.

9. Summary comparison

Table 21 provides a concise qualitative synthesis of the structural, numerical, and computational characteristics of the three methods. It complements the quantitative results reported in **Table 20**.

No single method is uniformly superior with respect to every criterion. SCTM and SCCM provide the highest approximation accuracy for the six benchmarks considered. SCCM is computationally more attractive than SCTM in the present implementation because it avoids the repeated weighted projection integrations while retaining comparable accuracy.

HWCM produces larger errors at the same balanced approximation size, but it consistently generates less dense and substantially better-conditioned systems. Its localized basis also gives regular algebraic convergence under balanced refinement.

Example 6 confirms that the accuracy of SCTM and SCCM is not solely a consequence of exact polynomial reproduction. Both methods retain high-order convergence for the nonpolynomial solution $u(x) = x^{5/2}$, whereas HWCM maintains first-order-type convergence together with markedly better conditioning and sparsity.

Table 21. Qualitative structural, numerical, and computational comparison of the three methods.

Criterion	SCTM	SCCM	HWCM
Basis and enforcement	Global shifted Chebyshev basis with weighted residual projection	Global shifted Chebyshev basis with pointwise residual enforcement at shifted Chebyshev–Gauss nodes	Localized piecewise-constant Haar basis with midpoint collocation
Fractional operators	Fractional derivatives of the shifted Chebyshev basis enter weighted projection equations	The same fractional-derivative representation is evaluated directly at collocation nodes	Fractional integration matrices reconstruct the solution and its required derivatives
Matrix structure	Predominantly dense; observed densities 0.942383–0.999023	Effectively dense; observed densities 0.999023–1.000000	More structured and less dense; observed density 0.593750 in all six experiments at $N = 32$
Observed conditioning	$\kappa_2(A)$ ranges from 3.54783×10^1 to 1.28946×10^6	$\kappa_2(A)$ ranges from 8.40856×10^1 to 3.14799×10^6	$\kappa_2(A)$ ranges from 3.69247 to 1.03747×10^1
Smooth polynomial benchmarks	Exact polynomial profiles are recovered to the adopted precision whenever they belong to the approximation space	Exact polynomial profiles are recovered to the adopted precision whenever they belong to the approximation space	Correct global profiles are recovered, but maximum errors remain of order 10^{-2} at $N = 32$
Low-regularity benchmark	Maximum error 4.39523×10^{-6}; final rate 3.40626	Maximum error 4.31475×10^{-6}; final rate 3.30022	Maximum error 4.33493×10^{-2}; final rate 1.04617
Observed convergence	Polynomial recovery in Examples 1–5 and high-order algebraic convergence in Example 6	Polynomial recovery in Examples 1–5 and high-order algebraic convergence in Example 6	Generally first-order-type algebraic convergence; a lower rate occurs in Example 2
Dominant computational step	Evaluation of weighted projection integrals	Residual and operator evaluation at collocation nodes	Construction and application of fractional integration matrices
Main advantage	High approximation accuracy with a direct weighted-residual interpretation	High approximation accuracy with substantially lower assembly cost than SCTM	Favorable conditioning, greater sparsity, and localized representation
Main limitation	High assembly cost and potentially large condition numbers	Dense matrices and potentially large condition numbers	Larger approximation errors at the same balanced approximation size

The appropriate method therefore depends on the required balance among accuracy, assembly cost, conditioning, sparsity, and solution regularity. The conclusions presented here apply to the selected benchmark problems and do not constitute a universal superiority statement for arbitrary fractional differential models.

10. Comparative discussion

The six benchmark problems provide a balanced comparison among SCTM, SCCM, and HWCM using the same approximation sizes,

$$N \in \{4, 8, 16, 32\},$$

the same numbers of unknown coefficients, and the same independent error grid. The numerical results reveal two distinct approximation regimes. Examples 1–5 have smooth polynomial exact solutions, whereas Example 6 has the nonpolynomial low-regularity solution

$$u_{\text{exact}}(x) = x^{5/2}.$$

10.1. Accuracy and convergence

For the polynomial solutions in Examples 1–5, SCTM and SCCM recover the exact profiles to the adopted working precision whenever the exact polynomial belongs to the selected shifted Chebyshev approximation space. The precision-level maximum and RMS errors in these cases result from finite-dimensional polynomial reproduction

and should not be interpreted as observed asymptotic convergence rates.

Example 6 provides a genuine convergence test because its exact solution is nonpolynomial and its third derivative is unbounded as $x \to 0^+$. At $N = 32$, SCTM and SCCM give maximum errors of

$$4.39523 \times 10^{-6} \qquad \text{and} \qquad 4.31475 \times 10^{-6},$$

respectively. Their corresponding RMS errors are

$$3.11477 \times 10^{-6} \qquad \text{and} \qquad 3.05058 \times 10^{-6},$$

while their final observed maximum-error convergence rates are 3.40626 and 3.30022.

For the same example, HWCM gives a maximum error of 4.33493×10^{-2}, an RMS error of 1.17675×10^{-2}, and a final observed rate of 1.04617. Thus, the shifted Chebyshev formulations retain high-order accuracy for the low-regularity benchmark, whereas HWCM exhibits regular first-order-type convergence.

10.2. Formulation and enforcement

SCTM determines the unknown coefficients through weighted residual projection equations together with the prescribed initial or boundary conditions. SCCM uses the same shifted Chebyshev trial space but enforces the residual directly at shifted Chebyshev–Gauss nodes. Consequently, SCCM avoids the projection integrals required by the Tau formulation.

HWCM follows a different construction. The highest required derivative is expanded in the localized Haar basis, and the solution and remaining derivative terms are reconstructed through operational matrices of fractional integration. Endpoint correction terms are included so that the prescribed initial conditions are satisfied independently of the unknown Haar coefficients.

10.3. Algebraic structure

The global support of the shifted Chebyshev basis produces predominantly dense coefficient matrices. At $N = 32$, the observed matrix densities range from approximately 0.942 to 1.000 for the Chebyshev formulations. By contrast, the HWCM density is 0.593750 in all six reported experiments, corresponding to a sparsity ratio of 40.625%.

The spectral two-norm condition numbers range from approximately 3.55×10^1 to 1.29×10^6 for SCTM and from approximately 8.41×10^1 to 3.15×10^6 for SCCM. The corresponding HWCM condition numbers remain between approximately 3.69 and 10.37. The Haar systems are therefore substantially better conditioned and less dense for the benchmark problems considered, although this structural advantage is accompanied by larger approximation errors at the same balanced size.

10.4. Computational cost

The linear-system solution times are similar for all three methods because the balanced systems have the same dimension. The dominant difference occurs during

matrix assembly. At $N = 32$, the total recorded times across the six examples range from approximately 4.81 to 173.20 seconds for SCTM, from 0.0165 to 0.0405 seconds for SCCM, and from 0.0228 to 0.0456 seconds for HWCM.

The comparatively large SCTM times result mainly from the evaluation of the weighted projection integrals. SCCM avoids these integrations and generally gives the lowest measured total cost. HWCM has a computational cost comparable to SCCM while retaining its favorable conditioning and reduced matrix density. These timings were obtained within the same Mathematica session and are interpreted as relative implementation-cost indicators rather than machine-independent performance measures.

10.5. Residual interpretation

The differential-equation residual and the solution error measure different numerical properties. The maximum and RMS errors quantify the distance between the numerical and exact solutions, whereas the differential-equation residual measures how closely the computed approximation satisfies the governing equation at the evaluation points.

Derivative-based residuals may be more sensitive than solution errors to endpoint regularity and numerical differentiation. Residual values should therefore be interpreted together with the solution errors, convergence histories, initial-condition residuals, and matrix diagnostics rather than being used alone to establish stability or method superiority.

10.6. Scope of the comparison

The numerical evidence establishes a clear accuracy–structure trade-off for the six benchmark problems. SCTM and SCCM provide the highest approximation accuracy, while HWCM produces better-conditioned and less-dense systems. SCCM combines the accuracy of the shifted Chebyshev approximation with a substantially lower measured assembly cost than SCTM.

These findings are restricted to the selected equations, fractional orders, approximation sizes, implementation procedures, and test grids. They do not establish a universal ranking for nonlinear, large-scale, strongly localized, or more severely nonsmooth fractional models. Such problems require separate balanced numerical investigations.

11. Conclusion

This paper presented a balanced computational comparison of three operational-matrix-based formulations for Caputo fractional differential equations: the Shifted Chebyshev Tau Method (SCTM), the Shifted Chebyshev Collocation Method (SCCM), and the Haar Wavelet Collocation Method (HWCM). Six benchmark problems with known exact solutions were examined using the common balanced approximation sizes

$$N \in \{4, 8, 16, 32\},$$

and the numerical errors were evaluated on the same independent test grid.

For the five smooth polynomial benchmarks, SCTM and SCCM recover the exact profiles to the adopted working precision whenever the exact solution belongs to the selected shifted Chebyshev approximation space. Although the Tau and collocation formulations enforce the governing equations differently, they recover the same polynomial coefficient representation in these cases.

The sixth benchmark has the nonpolynomial exact solution

$$u_{\text{exact}}(x) = x^{5/2},$$

which belongs to $C^2[0,1]$ but not to $C^3[0,1]$. All three methods therefore produce genuine nonzero approximation errors. At $N = 32$, the maximum errors of SCTM and SCCM are 4.39523×10^{-6} and 4.31475×10^{-6}, with final observed rates of 3.40626 and 3.30022, respectively. HWCM gives a maximum error of 4.33493×10^{-2} and a final observed rate of 1.04617.

The algebraic diagnostics reveal complementary behavior. The shifted Chebyshev formulations produce the smallest errors but generally lead to dense matrices with comparatively large condition numbers. HWCM produces larger errors at the same approximation size but gives less-dense and substantially better-conditioned systems.

The measured computational times also distinguish the two Chebyshev formulations. SCCM avoids the weighted projection integrals required by SCTM and generally achieves comparable accuracy with a much lower assembly cost. HWCM also has a low measured computational cost and benefits from the localized support of its basis functions.

No single formulation is therefore superior with respect to every criterion. For the problems studied, SCCM provides the most favorable accuracy–time balance, SCTM retains the weighted-projection structure of the Tau formulation, and HWCM offers favorable conditioning, reduced matrix density, localization, and regular algebraic convergence.

The conclusions are restricted to the six benchmark equations and the balanced numerical settings adopted in this study. Further work may consider nonlinear fractional equations, coupled systems, adaptive Haar resolutions, domain-decomposition strategies, and problems with stronger endpoint singularities or localized solution features.

Author contributions: Both authors contributed equally to the mathematical formulation, numerical analysis, interpretation of the reported results, and preparation of the manuscript. Both authors reviewed and approved the final version of the manuscript.

Funding: This research received no external funding. The article processing charge was paid by the authors.

Institutional review board statement: Not applicable.

Informed consent statement: Not applicable.

Data availability statement: This study did not involve the use of external or empirical datasets. All numerical results generated during the study and supporting its findings are presented within the article.

Conflict of interest: The authors declare that they have no financial or commercial interests that could have influenced the work reported in this manuscript.

AI use statement: During the preparation of this manuscript, the authors used ChatGPT (OpenAI) for language refinement, editorial restructuring, and drafting assistance. All mathematical derivations, numerical algorithms, Mathematica implementations, computed data, tables, figures, and scientific interpretations were independently checked, validated, and approved by the authors. No AI-assisted material was accepted without critical author review. The authors take full responsibility for the accuracy, integrity, and content of the manuscript.

References

1. Podlubny I. Fractional Differential Equations: An Introduction to Fractional Derivatives, Fractional Differential Equations, to Methods of Their Solution and Some of Their Applications. Academic Press; 1999.
2. Kilbas AA, Srivastava HM, Trujillo JJ. Theory and Applications of Fractional Differential Equations. Elsevier; 2006.
3. Diethelm K, Ford J. Numerical Solution of the Bagley-Torvik Equation. BIT Numerical Mathematics. 2002; 42(3): 490–507. doi: 10.1023/A:1021973025166
4. El-Mesiry AEM, El-Sayed AMA, El-Saka HAA. Numerical methods for multi-term fractional (arbitrary) orders differential equations. Applied Mathematics and Computation. 2005; 160(3): 683–699. doi: 10.1016/j.amc.2003.11.026
5. Zayernouri M, Karniadakis GE. Exponentially accurate spectral and spectral element methods for fractional ODEs. Journal of Computational Physics. 2014; 257: 460–480. doi: 10.1016/j.jcp.2013.09.039
6. Arikoglu A, Ozkol I. Solution of fractional differential equations by using differential transform method. Chaos, Solitons & Fractals. 2007; 34(5): 1473–1481. doi: 10.1016/j.chaos.2006.09.004
7. Atabakzadeh MH, Akrami MH, Erjaee GH. Chebyshev operational matrix method for solving multi-order fractional ordinary differential equations. Applied Mathematical Modelling. 2013; 37(20–21): 8903–8911. doi: 10.1016/j.apm.2013.04.019
8. Ali KK, El Salam MAA, Mohamed EM. Chebyshev operational matrix for solving fractional order delay-differential equations using spectral collocation method. Arab Journal of Basic and Applied Sciences. 2019; 26(1): 342–353. doi: 10.1080/25765299.2019.1629543
9. Baleanu D, Shiri B, Srivastava HM, et al. A Chebyshev spectral method based on operational matrix for fractional differential equations involving non-singular Mittag-Leffler kernel. Advances in Difference Equations. 2018; 2018(1): 353. doi: 10.1186/s13662-018-1822-5
10. Abdelkawy MA, Amin AZM, Lopes AM, et al. Shifted Fractional-Order Jacobi Collocation Method for Solving Variable-Order Fractional Integro-Differential Equation with Weakly Singular Kernel. Fractal and Fractional. 2021; 6(1): 19. doi: 10.3390/fractalfract6010019
11. Sadiq S, Rehman MU. ψ-shifted operational matrix scheme for fractional partial differential equations. Journal of Applied Analysis & Computation. 2022; 12(2): 497–516. doi: 10.11948/20210101
12. Farhood AK, Mohammed OH. Shifted Chebyshev operational matrices to solve the fractional time-delay diffusion equation. Partial Differential Equations in Applied Mathematics. 2023; 8: 100538. doi: 10.1016/j.padiff.2023.100538
13. Ahmed HM. Enhanced shifted Jacobi operational matrices of integrals: spectral algorithm for solving some types of ordinary and fractional differential equations. Boundary Value Problems. 2024; 2024(1): 75. doi: 10.1186/s13661-024-01880-0
14. Ahmed HM. Highly Accurate Numerical Method for Solving Fractional Differential Equations with Purely Integral Conditions. Fractal and Fractional. 2025; 9(7): 407. doi: 10.3390/fractalfract9070407
15. Ahmed HM, Izadi M, Cattani C. A Spectral Approach to Variable-Order Fractional Differential Equations: Improved

Operational Matrices for Fractional Jacobi Functions. Mathematics. 2025; 13(16): 2544. doi: 10.3390/math13162544
16. Mason JC, Handscomb DC. Chebyshev Polynomials. Chapman and Hall/CRC; 2002. doi: 10.1201/9781420036114
17. Canuto C, Hussaini MY, Quarteroni A, et al. Spectral Methods: Fundamentals in Single Domains. Springer Berlin Heidelberg; 2006. doi: 10.1007/978-3-540-30726-6
18. Oloniiju SD, Mukwevho N, Tijani YO, et al. Chebyshev Pseudospectral Method for Fractional Differential Equations in Non-Overlapping Partitioned Domains. AppliedMath. 2024; 4(3): 950–974. doi: 10.3390/appliedmath4030051
19. El-Sayed AA, Agarwal P. Spectral treatment for the fractional-order wave equation using shifted Chebyshev orthogonal polynomials. Journal of Computational and Applied Mathematics. 2023; 424: 114933. doi: 10.1016/j.cam.2022.114933
20. Babaei A, Banihashemi S, Moghaddam BP, et al. Hexic-Chebyshev Collocation Method for Solving Distributed-Order Time-Space Fractional Diffusion Equations. Axioms. 2025; 14(7): 515. doi: 10.3390/axioms14070515
21. Abdelgaber KM, Fathy M, Hassan A, et al. Computational study of fractional partial differential equations using the second-kind Chebyshev collocation technique with error analysis. Boundary Value Problems. 2026; 2026(1): 20. doi: 10.1186/s13661-025-02202-8
22. Abd-Elhameed WM, Abdelkawy MA, Alsafri NMA, et al. Numerical Treatment of the Time-Fractional Kuramoto–Sivashinsky Equation Using a Combined Chebyshev-Collocation Approach. Fractal and Fractional. 2025; 9(11): 727. doi: 10.3390/fractalfract9110727
23. Daubechies I. Ten Lectures on Wavelets. Society for Industrial and Applied Mathematics; 1992. doi: 10.1137/1.9781611970104
24. Lepik Ü. Numerical solution of differential equations using Haar wavelets. Mathematics and Computers in Simulation. 2005; 68(2): 127–143. doi: 10.1016/j.matcom.2004.10.005
25. Li Y, Zhao W. Haar wavelet operational matrix of fractional order integration and its applications in solving the fractional order differential equations. Applied Mathematics and Computation. 2010; 216(8): 2276–2285. doi: 10.1016/j.amc.2010.03.063
26. Shiralashetti SC, Deshi AB. An efficient Haar wavelet collocation method for the numerical solution of multi-term fractional differential equations. Nonlinear Dynamics. 2016; 83(1–2): 293–303. doi: 10.1007/s11071-015-2326-4
27. Abdeljawad T, Amin R, Shah K, et al. Efficient sustainable algorithm for numerical solutions of systems of fractional order differential equations by Haar wavelet collocation method. Alexandria Engineering Journal. 2020; 59(4): 2391–2400. doi: 10.1016/j.aej.2020.02.035
28. Amin R, Alshahrani B, Mahmoud M, et al. Haar wavelet method for solution of distributed order time-fractional differential equations. Alexandria Engineering Journal. 2021; 60(3): 3295–3303. doi: 10.1016/j.aej.2021.01.039
29. Saha Ray S. On Haar wavelet operational matrix of general order and its application for the numerical solution of fractional Bagley Torvik equation. Applied Mathematics and Computation. 2012; 218(9): 5239–5248. doi: 10.1016/j.amc.2011.11.007
30. Mechee MS, Al-Shaher OI, Al-Juaifri GA. Haar wavelet technique for solving fractional differential equations with an application. AIP Conference Proceedings. 2019; 2086: 030025. doi: 10.1063/1.5095110
31. Shah K, Khan ZA, Ali A, et al. Haar wavelet collocation approach for the solution of fractional order COVID-19 model using Caputo derivative. Alexandria Engineering Journal. 2020; 59(5): 3221–3231. doi: 10.1016/j.aej.2020.08.028
32. Bulut F, Oruc O, Esen A. A 3-Scale Haar Wavelet Collocation Method for Numerical Solution of the Nonlinear Gardner Equation. Mediterranean Journal of Mathematics. 2025; 22(2): 38. doi: 10.1007/s00009-025-02808-3
33. Amin R, Shah K, Ahmad H, et al. Haar wavelet method for solution of variable order linear fractional integro-differential equations. AIMS Mathematics. 2022; 7(4): 5431–5443. doi: 10.3934/math.2022301
34. Amin R, Ullah R, Khan I, et al. Haar wavelet method with Caputo derivative for solution of a system of fractional integro-differential equations. Journal of Applied Analysis & Computation. 2025; 15(3): 1641–1658. doi: 10.11948/20240325
35. Hamood MM, Sharif AA, Ghadle KP. A unified Haar wavelet collocation framework for fractional Volterra integro-differential equations with application to tumor-immune dynamics modeling. Scientific Reports. 2026; 16(1): 12552. doi: 10.1038/s41598-026-42803-6
36. Yi M, Huang J. Wavelet operational matrix method for solving fractional differential equations with variable coefficients. Applied Mathematics and Computation. 2014; 230: 383–394. doi: 10.1016/j.amc.2013.06.102
37. Gupta S, Ranta S. Legendre wavelet based numerical approach for solving a fractional eigenvalue problem. Chaos, Solitons & Fractals. 2022; 155: 111647. doi: 10.1016/j.chaos.2021.111647
38. Suganthi J, Maury SC. A wavelet-based collocation approach for solving chlorine transport model. Boundary Value

Problems. 2026; 2026(1): 108. doi: 10.1186/s13661-026-02273-1

39. Chen Y, Yi M, Yu C. Error analysis for numerical solution of fractional differential equation by Haar wavelets method. Journal of Computational Science. 2012; 3(5): 367–373. doi: 10.1016/j.jocs.2012.04.008
40. Majak J, Shvartsman B, Pohlak M, et al. Solution of fractional order differential equation by the Haar Wavelet method. Numerical convergence analysis for most commonly used approach. AIP Conference Proceedings. 2016; 1738: 480110. doi: 10.1063/1.4952346